frontiers | Frontiers in Soft Matter

TYPE Original Research
PUBLISHED 08 September 2023
DOI 10.3389/frsfm.2023.1240878

OPEN ACCESS

EDITED BY
Jordi Ignés-Mullol,
University of Barcelona, Spain

REVIEWED BY
Natalia Wilke,
National University of Cordoba
(CIQUIBIC), Argentina
Aaron Elbourne,
RMIT University, Australia

*CORRESPONDENCE
Thomas Hellweg,
✉ thomas.hellweg@uni-bielefeld.de
Francisco Monroy,
✉ monroy@ucm.es

RECEIVED 15 June 2023
ACCEPTED 22 August 2023
PUBLISHED 08 September 2023

CITATION
Moleiro LH, Martín-Romero MT,
Herráez-Aguilar D, Santiago JA, Caselli N,
Dargel C, Geisler R, Hellweg T and
Monroy F (2023), Dual mechanical impact
of β-escin on model lipid membranes.
Front. Soft Matter 3:1240878.
doi: 10.3389/frsfm.2023.1240878

Dual mechanical impact of β-escin on model lipid membranes

Lara H. Moleiro[1,2], María T. Martín-Romero[3],
Diego Herráez-Aguilar[4], José A. Santiago[5], Niccolò Caselli[1,2],
Carina Dargel[2,6], Ramsia Geisler[2,7], Thomas Hellweg[2]* and
Francisco Monroy[1,8]*

[1]Departamento de Química Física, Universidad Complutense de Madrid, Madrid, Spain, [2]Fakultät für Chemie, Physikalische und Biophysikalische Chemie, Universität Bielefeld, Bielefeld, Germany, [3]Departamento de Química Física y T. Aplicada and Instituto Químico para la Energía y el MedioAmbiente. Universidad de Córdoba, Córdoba, Spain, [4]Facultad de Ciencias Experimentales, Universidad Francisco de Vitoria (UFV), Madrid, Spain, [5]Departamento de Matemáticas Aplicadas y Sistemas, Universidad Autónoma Metropolitana Cuajimalpa, Ciudad de México, Mexico, [6]Institut für Physikalische Chemie, Universität Münster, Münster, Germany, [7]Innere Medizin II, Hämatologie/Onkologie, Goethe-Universität, Frankfurt, Germany, [8]Biofísica Traslacional, Instituto de Investigación Sanitaria, Hospital 12 de Octubre (imas12), Madrid, Spain

Understanding the mechanical behavior of biological membranes is of paramount importance in cell biophysics and in developing new biomaterials for medicine. In this study, we delve into the mechanical impact of β-escin, commonly referred to as escin, a naturally occurring biosurfactant derived from the seeds of the horse chestnut tree. To examine the modulable interaction between escin and dimyristoylphosphatidylcholine (DMPC), which is an archetypical fluid phospholipid and an essential constituent of the cellular fluid membrane, we have used artificial models based on the liquid crystal structure, such as bilayer vesicles and Langmuir monolayers. We have focused on the energetic and kinetic aspects of escin insertion when transversally adsorbed or longitudinally integrated within these model membranes. By employing surface microscopies of epifluorescence and Brewster angle reflectivity, we have elucidated the structural phase behavior of hybrid escin–phospholipid membranes, which exhibit dual mechanical properties characterized by high rigidity and reduced fluidity. Notably, at low temperatures, we observe a soft, glassy rheological behavior reminiscent of liquid crystalline ordered phases, which turns into a fluid-like viscoelasticity resembling more disordered phases at physiological temperatures. The hybrid membranes behave in one way or another as both are driven by an adsorption potential well imposed by escin cohesivity. These intriguing findings are discussed from a physicochemical perspective, highlighting their potential for future pharmacological designs and biomedical applications that exploit the dual mechanical impact of escin on biological membranes.

KEYWORDS

β-escin, membrane phospholipids, model lipid membranes, Langmuir monolayers, bilayer vesicles, adsorption kinetics, fluorescence microscopy, Brewster angle microscopy

1 Introduction

The fluid mosaic paradigm is a structural concept that describes biological membranes as flexible objects with lateral molecular mobility (Singer and Nicolson, 1972). The heterogeneous mosaic-like composition allows embedded membrane proteins to move laterally within lipid domains that are dispersed in a continuous liquid phase (Simons and Ikonen, 1997). Although flexible membranes resist shear deformations as solids, they flow as incompressible liquids under applied shear stress. Biological membranes require structural rigidity and lateral fluidity, combining the solid-like and liquid-like characteristics, to maintain functional homeostasis (Sprong et al., 2001; Van Meer et al., 2008; Philips et al., 2009). Two previous pivotal studies have hypothesized that this mechanical duality arises from the viscoelastic nature of the proteolipid membrane, which is mainly influenced by the heterogeneous composition of the constituent lipid monolayers (Evans and Hochmuth, 1976; Espinosa et al., 2011). The dual viscoelasticity of biological membranes, characterized by high dynamic viscosity for regulated fluidity and a finite shear modulus for structural resistance (López-Montero et al., 2008), is supported by the liquid crystalline arrangement of membrane lipids (López-Montero et al., 2010; Catapano et al., 2011; Castro et al., 2014; Hermans and Vermant, 2014). Experimental studies with real cells have further substantiated the viscoelastic duality hypothesis of biological membranes as regulated by lipid traffic flows (Catapano et al., 2017; Deseri and Steigmann, 2017; Alonso and Goñi, 2018; Le Roux et al., 2019; Xu et al., 2020). For instance, metabolic conversions of fluid sphingomyelins into solid ceramide led to lateral tension Marangoni gradients (Catapano et al., 2017; Alonso and Goñi, 2018), resulting in cell shape transformations with a functional significance (López et al., 2012). Furthermore, lipid membranes have the functional capacity to propagate mechanical signals, playing a crucial role in cellular mechanobiology (Le Roux et al., 2019; Mussel and Schneider, 2019). Moreover, membrane viscoelastic stresses have been implicated in cancer development (Tse et al., 2012; Xu et al., 2020) and phenotypic cell hereditariness (Deseri and Steigmann, 2017; Vorselen et al., 2018). Despite the important advances in understanding the functional dynamics of biomembranes through experimental models (López-Montero et al., 2008; Arriaga et al., 2009; Arriaga et al., 2010a; López-Montero et al., 2010; Catapano et al., 2011; Espinosa et al., 2011; Schmid, 2013; Castro et al., 2014; Hermans and Vermant, 2014; Hormel et al., 2014; Langevin and Monroy, 2014; Wu et al., 2015; Catapano et al., 2017; Al-Rekabia and Contera, 2018) and the relevant theoretical approaches related to their liquid crystalline viscoelasticity (Helfrich, 1973; Lipowsky, 1991; Seifert, 1997; Arriaga et al., 2008; Rahimi and Arroyo, 2012; Mell et al., 2015; Santiago et al., 2019; Liu and Kim, 2020; Santiago and Monroy, 2020), our current understanding of the mechanical paradigm of biological membranes remains incomplete, particularly regarding the molecular impacts of order-imparting components on membrane stresses. Here, we present a rheological investigation of the order-imparting molecule β-escin, a saponin biosurfactant that mimics the effects of solid-like mechanical stresses in model phospholipid membranes. We have analyzed the surface rheology of these membrane models by recording the solid saponin molecule (β-escin) while simultaneously enhancing surface stiffness but dropping viscous friction (Sreij et al., 2017; Kharbedia et al., 2021). Dual mechanical effects have been discriminated in two differential structural scenarios: longitudinal escin integration mimicking intrinsic lateral membranogenesis or transverse escin insertion after bulk diffusion recapitulating extrinsic membrane traffic. Such mechanical duality as a high stiffness followed by high fluidity, and the emergent properties tunable therefrom, confer β-escin in particular and saponins in general with two scopes of applicability, biotechnological as novel biosurfactants with singular surface rheology imparting thermodynamic stability without loss of mechanical performance (Böttcher and Drusch, 2017) and biomedical as natural therapeutic agents targeting cell membrane rigidness being a key regulator of inflammation (Sirtori, 2001; Lorent et al., 2014).

Saponin biosurfactants: from molecular amphiphile structure to biomedical applications, through of physicochemical modelling in viscoelastic membranes

Natural saponins are a family of triterpenoid saccharides present in many common plants, such as potatoes, beans, soy, and ginseng (Hostettmann and Marston, 1995). They can also be obtained from phytochemical extracts of several medicinal plants, including *Quillaja saponaria*, *Yucca schidigera*, *Saponaria officinalis*, and *Aesculus hippocastanum* (Sparg et al., 2004; Cheok et al., 2014). Because of their self-assembly and surface-active behavior at aqueous interfaces, they endow emulsifier and foaming activities in aqueous media (Böttcher and Drusch, 2017; Geisler et al., 2020a). Their biochemical classification as biosurfactants makes them useful for the technological development of functional foods, cosmetics, phytosanitary products, and natural drugs (Güçlü-Ustündağ and Mazza, 2007; Böttcher and Drusch, 2017). Particularly, β-escin(*aka escin*), the major saponin component extracted from the chestnut seed of *A. hippocastanum*, is currently being exploited as a convenient biosurfactant in a variety of technological applications (Hostettmann and Marston, 1995; Sparg et al., 2004; Güçlü-Ustündağ and Mazza, 2007; Cheok et al., 2014; Böttcher and Drusch, 2017; Geisler et al., 2020a). This triterpenoid derivative of glucopyranosic acid has the chemical formula shown in Figure 1A, which reveals the amphiphilic molecular structure discernible as an oligosaccharide flexible subsystem—the glyconic saccharide constituting the polar head—which is linked to a triterpene core ring planar subsystem—the aglycone constituting the hydrophobic moiety (see Figure 1A; inset). The glyconic part contains glucose and glucuronic acid, both hydrophilic, whereas several polar oxygen groups are attached to the aglyconic part. They appear one-sided in the triterpene, thus conferring lateral (longitudinal) polarity additional to the conventional (transverse) surfactant-like bipolarity (De Groot et al., 2018). This quadrupolar amphipilic structure confers high solubility followed by enhanced hydrophilicity responsible for a relatively high critical micellar concentration ($CMC \approx 0.4\, mM$; practically independent of temperature) (De Groot et al., 2018; Dargel et al., 2019). The high surface orientability of the quadrupolar escin molecule enables hydrogen bonding in transverse and longitudinal insertion directions (Dargel et al., 2019; Geisler et al., 2020a).

In structural terms referred to the adsorption compaction status at aqueous membrane interfaces, the amphiphilic quadrupolar nature of escin outfits with its potential ability to further interact longitudinally with other amphipathic membrane partners (Sreij et al., 2017; Glickman et al., 2020; Kharbedia et al., 2021). These extraordinary (in-plane) intrinsic interactions are superposed to ordinary (out-of-plane) extrinsic adsorption, thus causing

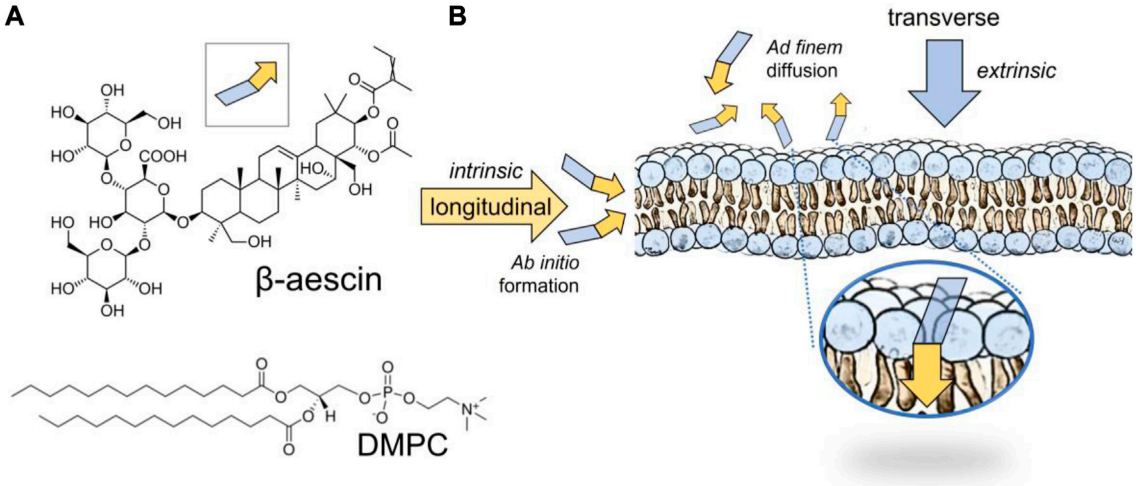

FIGURE 1
(A) Chemical formula of β-escin, or simply *escin* (MW 1,131.26 g/mol). Notice the quadrupolar structure of the molecule with a polar head constituted by a trisaccharide sugar (blue trapezoid) and a laterally amphiphilic moiety of pentacyclic terpenoid, an aglycone basis prone to membrane insertion under lateral stacking (yellow arrow). DMPC is the structural phospholipid chosen to recapitulate a fluid and flexible membrane. **(B)** Structural scenarios for saponin membrane incorporation under lateral stacking. The intrinsic integration corresponds to *ab initio* incorporation in the endogenous composition (i.e., before membrane formation, also referred to as longitudinal escin integration). The extrinsic insertion scenario corresponds to *ad finem* incorporation under exogenous adsorption (i.e., after membrane formation, also referred to as transverse escin insertion). Adsorption mechanism: 1) escin first interacts hydrophilically with the outer membrane through the polar phospholipid heads; 2) once adsorbed, it reorganizes hydrophobically with the terpenoid ring embedded by lateral stacking in the organic core of the lipid membrane; see zoomed inset for final equilibrium insertion. Both scenarios are comparatively studied.

additional mosaic membrane ordering by lateral membrane stacking mediated by the amphiphilic terpenoid moiety interacting with other membrane phospholipids, sphingolipids and cholesterol (Sreij et al., 2017; Sreij et al., 2019; Geisler et al., 2020a; Geisler et al., 2020b). The formation of surface-structured films in some saponin extracts, other than escin, has been revealed to be concomitant with compact hydrophobic domains attributed to additional hydrogen bonding between sugar residues (e.g., in triterpenoid saponins of oleanane or dammarane aglycone type) (Böttcher and Drusch, 2017; Geisler et al., 2020a). Furthermore, some structural viscoelastic relationships have been derived between the botanical origin of the different saponins and their interfacial behavior, as determined by the formation of hydrophobic surface domains laterally compacted under hydrogen bond stacking (Golemanov et al., 2013; Böttcher et al., 2017). In particular, the most stable films were identified for saponins of oleanane type as mesoscopic shear rigidity is mediated by static solid domains rapidly formed at equilibrium (Golemanov et al., 2014).

Saponins with different botanic origins exhibit a variety of biological activities, such as natural antibiotics and biocides (Miyakoshi et al., 2000; Sparg et al., 2004). Moreover, some cytotoxic effects and anti-tumorigenic potentials have been shown on cancer cells treated with certain saponins, including β-escin (Lorent et al., 2014; Koczurkiewicz et al., 2015; Elekofehinti et al., 2021). However, their propensity to induce systemic hemolysis limits toxicological safety in cancer therapies (Sirtori, 2001; Gauthier et al., 2009). Saponins are included among a class of natural medicines called phlebotonics, which are used to treat thrombophlebitis and other venous insufficiencies, mainly varicose veins of the legs and hemorrhoids (Sirtori, 2001). They can be safely administrated by ingestion or topical application, and depending on the dose, they produce different phlebotonic effects, such as imparting rigidity and fluidity into the cellular membranes of the venous endothelial walls (Sirtori, 2001; Lorent et al., 2014; Gwozdzinski et al., 2023). Particularly referring to β-escin extracted from chestnut seeds (*A. hippocastanum*), anti-inflammatory, anti-edematous, and venotonic effects have been attributed to this natural compound (Sirtori, 2001; Gallelli, 2019). Many clinical studies have been conducted to date (Underland et al., 2012), specifically confirming escin as a safe and effective phlebotonic to treat chronic venous insufficiency (CVI) (Pittler and Ernst, 2012; Dudek-Makuch and Studzińska-Sroka, 2015). In pathophysiological terms, the escin-based regulation of cell membrane rigidness seems to be the key factor for reducing varicose inflammation (Gwozdzinski et al., 2023). Although the etiology of inflammatory venous diseases is very complex, it involves genetic susceptibility, cellular responses, and environmental factors that cause vein wall inflammation, such as hypoxia, abnormal flow stresses, and venous blood stasis elicited by altered levels of nitric oxide and prostaglandins in circulation (Smith et al., 2006; Cogolludo et al., 2019). The mechanical status of membrane stiffness and fluidity in the venous endothelium, its glycocalyx, and the circulating blood cells is expected to be critical for determining the pathophysiological changes that occur in the venous bloodstream, for the expression of membrane-receptor cytokines and other cell adhesion molecules necessary for normal venous circulation. Despite the evident etiological involvement of altered membrane mechanics (Gallelli, 2019; Gwozdzinski et al., 2023), the possible pathogenic role of altered membrane fluidity remains unidentified. Therefore, studying the rheological impacts of escin on model biomimetic membranes is of utmost importance for assessing phlebotonic potentials, not only for CVI treatments, but also in other venous inflammatory diseases, considering cell membrane rigidness, fluidity, and adhesivity as therapeutic targets potentially modulable by the surface action of this saponin.

In this study, we have explored the mechanical influence of surface-structuring escin in model viscoelastic membranes reconstituted under compositional mosaicity, particularly in Langmuir monolayers and bilayer vesicles composed of the zwitterionic phase-segregating phospholipid dimyristoylphosphatidylcholine (DMPC). By exploiting the DMPC mesogenic transition between liquid crystal bilayer phases (from the ordered gel L_O-phase near room temperature to the disordered Lα-phase at $T_m \approx 24^{\circ}C$), the resulting mosaic model membranes (cf. phase-separated monolayers and bilayers) recapitulate all in one structural resilience, mesoscopic fluidity, and flexibility as tuned in terms of composition and temperature. As depicted in Figure 1B, a minimal biomimicry essentially captures a simplified membrane in which escin can be incorporated either intrinsically within the lipid composition before membrane formation (longitudinal integration) or extrinsically as an exogenous adsorption from the external aqueous suspension after membrane formation (transverse insertion). To assimilate comparable results, we have invoked Marsh's correspondence principle, by which equivalent states of bilayers and monolayers can be investigated for given components contributing the same free energy per unit area (Marsh, 1996). Under mechanical equilibrium, the bilayer packing equals the monolayer pressure corresponding to the ordered liquid condensed status; this is $\pi_b \approx 30 mN/m$—the bilayer—equivalent surface pressure (Helfrich, 1973; Lipowsky, 1991; Marsh, 1996; Espinosa et al., 2011). Hence, the simplest Langmuir monolayers will be exploited as minimalistic membrane models for discriminating the spatiotemporal scales of mosaic organization in which escin operates dually either when intrinsically incorporated into the membrane or when extrinsically adsorbed from the aqueous phase. In previous studies using neutron spin echo (NSE) and dynamic light scattering (DLS) with large unilamellar vesicles prepared by extrusion (LUVs), we have formerly shown how paradoxically escin causes domain segregation in rigid DMPC bilayers but leads to membrane softening by eliciting mesoscopic disorder under phase separation (Sreij et al., 2017; Geisler et al., 2020b). In phenomenological terms, such membrane impacts of escin are similar to the cholesterol effects imparting membrane disorder into saturated phospholipids (Finegold, 1992). Here, we go beyond those indirect signs of mechanical escin impact, and by combining newer kinetic data on membrane incorporation using surface microscopies (BAM and epifluorescence), together with surface rheology measurements, we have provided evidence on the existence of rigid domains composed of escin crystallites. Although these intrinsically structured domains should endow rigidness in the microscale, they could promote mesoscopic disorder, leading to extrinsic softening. By considering the two insertion scenarios revealed in LUVs (Sreij et al., 2017; Geisler et al., 2020b), we have assessed molecular compactions and mesoscopic phase disruptions of escin incorporated into DMPC bilayers reconstituted in giant unilamellar vesicles (GUVs). Furthermore, the resulting mechanics of the single membrane leaflets have been explored in the corresponding Langmuir monolayers containing escin as differentially inserted along extrinsic or intrinsic pathways. The solid-like domains mainly composed of escin have been demonstrated to trigger dual membrane mechanics tunable upon controlling the status of escin insertion.

2 Experimental: materials and methods

2.1 Chemicals

The purified molecule β-D-glucopyranosyl-(1→2)-[β-D-glucopyranosyl-(1→4)]-(22α-(acetyloxy)-16α,24,28-trihydroxy-21β-{[(2Z)-2-methylbut-2-enoyl]oxy}olean-12-en-3β-yl(β-D-glucopyranosidu-ronic acid), shortly named β-escin, was purchased from Sigma [purity grade as a pharmaceutical primary standard) and used without further purification (M.W. 1,131.26 g/mol). Escin was dissolved in ultrapure Milli-Q water (0.1 mM final submicellar concentration; $CMC \approx 0.3\,mM$) (De Groot et al., 2018). The fully saturated phospholipid 1,2-dimyristoyl-sn-glycero-3-phosphatidylcholine (DMPC) and the associated lipophilic dye 1,2-dioleoyl-sn-glycero-3-phosphoethanolamine-N-(lissamine-rhodamine B sulfonyl) (ammonium salt) (RhPE) were supplied by Avanti Polar Lipids. RhPE is labeled on the head group with the red-fluorescent rhodamine B fluorophore with excitation–emission maxima at 560/580 nm. The long-excited lifetime, small photobleaching, and low quenching make this dye ideal for the kinetics assays in aqueous environments. The unsaturated tails and the large head size locate RhPE in a water-rich region near the lipid headgroups at optimal interaction with other phospholipids in the disordered Lα-phase that is completely excluded from the ordered phases (Singh et al., 2016). The used lipids were dissolved in a chloroform–methanol mixture (3/1 v/v) to achieve a final concentration of 0.1 mg/ml DMPC for experiments with Langmuir monolayers or 1 mg/mL DMPC for preparing GUVs (0.1% w/w RhPE). The stock lipid solutions were stored at −20 °C. All other chemicals were obtained from Merck-Sigma. Ultrapure water was obtained from a Milli-Q system to constitute the aqueous subphase (Millipore, resistivity higher than 18 MΩ cm, organic residual lower than 1 ppb, surface tension 72.6 mN/m at 20 °C). The experiments were performed in water subphases buffered with 50 mM phosphate (PBS buffer pH 7.0).

2.2 Escin monolayer penetration

To measure penetration pressures in adsorption monolayers at the air/water (A/W) interface, we used a computer-controlled Langmuir trough (KSV/NIMA, small, 77.5 cm^2, Biolin Scientific Holding Ab, Stockholm, Sweden). By using a paper Wilhelmy-type sensor and two mobile barriers fabricated in Teflon®, the Langmuir trough is equipped with a pressure-area measuring system, $\pi(A;c) = \gamma_0 - \gamma(A;c)$ ($\gamma(A)$ is the actual surface tension, and γ_0 is the bare surface tension of the uncovered A–W interface). The absolute zero pressure is fixed under surface purity conditions assured for a bare surface repeatedly cleaned till constant pressure (i.e., $\pi = 0$ corresponds to $\gamma_0 = 72 mN/m$, measured for the largest area of the Langmuir trough; $A_0 = 7.5\,cm^2$ for barriers completely opened). To form the Langmuir lipid monolayer, a small amount of DMPC was dissolved in the chloroform–methanol mixture (1:1 v/v; 0.1 mg/ml). DMPC was then dropped at the A–W interface, and the monolayer was left to equilibrate by allowing the solvent to evaporate (approx. 30 min). The DMPC monolayers were considered for different initial statuses $\pi_0 (A; c = 0)$. In extrinsic adsorption experiments, the aqueous subphase (50 mM phosphate buffer) was exchanged with a solution of escin ($c = 0.1\,mM$ in phosphate buffer) using a peristaltic pump connected outside the barriers. Surface pressure *versus* time measurements were recorded until a constant surface pressure was reached. Experimental replicas were performed in triplicate. The results analyzed correspond to their arithmetic averages, and the experimental error is evaluated on the basis of the standard deviation of the sampled replicas (SD 10% typ.). The experiments were performed at 4°C (low-T experiments) or 38°C (high-T experiments).

2.3 Monolayer structure: Brewster angle and epifluorescence microscopy

Brewster angle microscopy (BAM) imaging revealed the internal structure of the monolayer at the micrometric level. BAM measurements were performed in a Langmuir trough installed on an I-Elli2000 ellipsometry station equipped with a Nd:YAG diode laser ($\lambda = 532\,nm$ wavelength; 50 mW power; Accurion GmbH). An incidence Brewster angle was chosen to maximize the reflected intensity and polarization sensibility ($\theta = 55.2^\circ \pm 0.1^\circ$). For a P-polarized beam incident at the Brewster angle, the reflected light can be expressed using the approximate Drude equation (Azzam and Bashara, 1992; Lheveder et al., 2000):

$$R_P(L,n) \approx \left(\frac{\pi L}{\lambda}\right)^2 \frac{n_1^2 + n_2^2}{\left(n_2^2 - n_1^2\right)^2} \left[\frac{\left(n^2 - n_1^2\right)\left(n_2^2 - n^2\right)}{n^2}\right]^2,$$

in terms of the surface film thickness (L) and refractive index (n) for the refractive indices of air ($n_1 = 1.000$) and the aqueous subphase ($n_2 = 1.333$).

Hence, the bare A/W interface appeared homogeneously black under the BAM (if $n = n_2$, then $R_P^{(0)} = 0$). However, for a heterogeneous surface film, the higher the optical contrasts, the whiter (i.e., if $n > n_2$, then $R_P > 0$). We estimated tailed phospholipids $n_{PC} \approx 1.41$ and the hydrophobic aglycone in escin $n_{esc} \approx 1.71$ as the glyconic saccharide was optically unmatched (WH de Jeu, 1980). Consequently, the brighter regions corresponded to the thicker optically contrasted areas of the monolayer, whereas the darker regions corresponded to locally thinner structures (or no presence of monolayer). The reflectivity analysis in the BAM I-Elli2000 image processing included a geometrical correction for spherical aberration and filtering to reduce interference fringes and noise. The BAM images were recorded simultaneously using the surface pressure monitorization. The I-Elli2000 station was equipped with an epifluorescence microscope.

2.4 Hydrostatic compression isotherms: compression modulus

We measured the isothermal compression modulus of the surface film as $K = -A(\partial\pi/\partial A)_T$. To ensure hydrostatic conditions, we exploited the previously described conical cup device (Catapano et al., 2011). The Langmuir monolayers were formed as described in Section 2.2. Once the spreading equilibrium was reached (at π_0), the surface area available to the monolayer was progressively reduced by lifting up the conical cup, whereas the surface pressure was measured at the center of the trough using a paper Wilhelmy plate attached to a force sensor (PS4, NIMA). This device allowed the measurement of surface pressure as $\pi(A,c) = \pi_0(A) + K(\pi,c)\Delta A/A$, under the isotropic compression produced by the radial contraction of the surface area $\Delta A/A$. The temperature was measured using a Pt-100 sensor and controlled by recirculating thermostated water (PolyScience). The conical trough was placed in a plexiglass box to avoid undesirable air streams or dust deposition on the surface during the experiments. Experimental replicas were performed in triplicate, and the analyzed results corresponded to arithmetic averages.

2.5 Monolayer viscoelasticity: interfacial shear rheology

We measured two-dimensional shear modulus ($\tilde{G} = G' + iG''$) using a double-wall rheometer under thermostatic and evaporation control (DWR ARES-G2). The Langmuir monolayers were formed as described in Section 2.2. The system was tempered at 4°C and left to equilibrate overnight. Subsequently, the temperature was adjusted. For low-T measurements, the experiments were maintained at 4°C. For high-T measurements, the subphase was slowly heated to 38°C (temperature sweep +10°C/h). The axial tensional stress in the samples was tracked permanently, and measurements were only performed when the mean stress reached a constant value. Experimental replicas were performed in triplicate, and the analyzed results corresponded to arithmetic averages.

2.6 Giant unilamellar vesicles

GUVs were prepared using the electroformation method according to the optimized protocol described by Mathivet et al. (1996). To prepare the GUVs, the lipid powder was first dissolved (at 1 mg/ml) in a chloroform–methanol mixture (2:1 v/v), then a drop of 20–30 μL was deposited on the ITO slide, and finally, the solvent was removed by evaporation in a stream of dry nitrogen. To prepare the GUVs of DMPC in the fluid state, we assembled ITO chambers first filled with an aqueous sucrose solution (200 mM) and then placed them inside an oven at ca. 38°C, well above the melting temperature of the phospholipid ($T_m = 23.6^\circ C$). Afterward, the sealed electroformation chambers were connected to an electric field for 3 h (8 Hz, 1.8 V). For subsequent GUV visualization under an optical microscope, the GUV sample previously electroformed in sucrose was further diluted in a glucose solution at a slightly higher concentration (208 mM). Such density contrast properly favored GUV sedimentation and visualization near the microscopy slide. For intrinsic integration assays (*ab initio* method), escin dissolved in methanol was admixed with the phospholipid solution in chloroform (30% w/w escin with respect to DMPC). For extrinsic insertion assays (*ad finem*

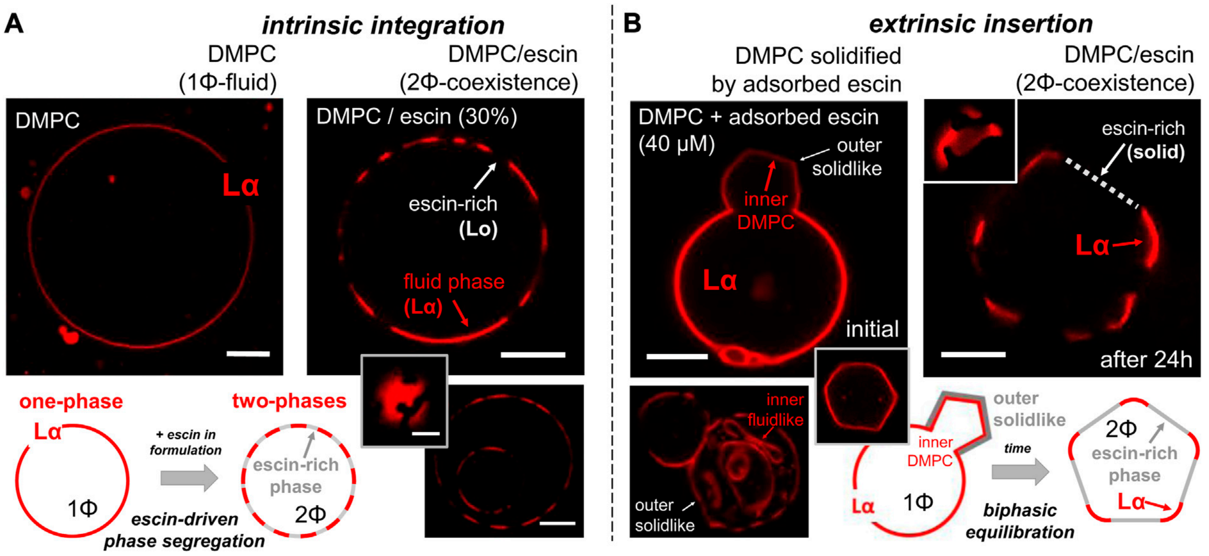

FIGURE 2
Confocal microscopy images obtained on the escin-integration/insertion scenarios as designed in Figure 1B for electroformed giant unilamellar vesicle (GUV) membranes. The microscopy observations were performed at room temperature (ca. 22°C). Under the considered experimental conditions, the fluorescent phospholipid dye RhPE was selective for the fluid-disordered phospholipid Lα-phase and excluded from the L_O-phase (see Section 2). Scale bars: 2 microns. **(A)** Intrinsic escin integration (*ab initio*) or longitudinal phase-separation scenario in which escin is included within DMPC before GUV electroformation. (Left panel) A pure DMPC vesicle in the homogeneous liquid-disordered phase (Lα). (Right panels) A hybrid, phase-separated ($L\alpha-L_O$) vesicle as electroformed from the DMPC−escin mixture (30% w/w.). (Inset) Zenithal view of a $L\alpha-L_O$ separated vesicle showing circular L_O-domains in Lα-continuous. (Bottom) Two "matrioska" vesicles appear with the same heterogeneous $L\alpha-L_O$ phase segregated configuration. **(B)** Extrinsic escin insertion (*ad finem*), or transverse phase-separation scenario in which escin is membrane inserted under adsorption from the suspending medium after DMPC GUVs are electroformed. (Left panels) Initial transformation stage, thereby a pure DMPC vesicle in the fluid Lα-phase becomes deformed under the action of a solid top layer locally adsorbed after 1 h incubation [in 40 μM escin, below CMC]. (Inset) Polygonal edge profile of a solidified GUV under rigidization by an escin top layer. (Bottom) Matrioska vesicles with the outer membrane rigidized in contact with escin, thus appearing solid-like (flat edges). The inner membranes remain fluid-like as becoming flexibly adapted to the inner space (rounded edges). (Right panel) Final equilibrium of the DMPC−escin vesicles as being $L\alpha-L_O$ phase-separated (after 24 h of escin-incubation). Once adsorbed and further reorganized, the escin-rich L_O-domains appear as flat edges excluding the fluorescent dye. The DMPC-rich Lα-phase adapts the rigid flat domains as a continuous flexible junction (see inset). Schematics: The bottom panels systematize the observed behavior in each insertion scenario.

method), a solution of escin monomers was added after the DMPC vesicles were electroformed in the suspending medium (40 μM final submicellar concentration) (De Groot et al., 2018). For fluorescence microscopy, a small amount of RhPE was added (0.1% w/w with respect to DMPC). Confocal microscopy observations were performed at room temperature.

3 Results

3.1 Intrinsic escin integration elicits molecular ordering in fluid DMPC-based membranes

From previous studies, escin is known to lead to the formation of solid domains when incorporated into fluid membranes (*ab initio* method) (Sreij et al., 2017; Geisler et al., 2020b; Glickman et al., 2020). It structurally behaves as integrated into the membrane composition through membrane biogenesis (see Figure 1; intrinsic longitudinal integration). To evaluate such longitudinal insertion in GUVs composed of a fluid DMPC membrane (at high temperature $T = 38\,^{\circ}C > T_m$), we exploited the fluorescence emission of RhPE, a lipophilic fluorescent dye that can conjugate to fluid phospholipid phases (Baumgart et al., 2007). Because the incorporation of escin triggers phase segregation into ordered arrangements (Sreij et al., 2017; Sreij et al., 2019), the fluorescent probe is excluded from the escin-rich ordered phases (e.g., gel-like and crystalline solid phases). As assessed by confocal microscopy, Figure 2A shows the formation of monophasic GUVs (1Φ) as revealed by the homogenous distribution of the RhPE dye (Figure 2A; left panel). However, the intrinsic integration of escin into binary GUVs was observed to partition into a biphasic coexistence (2Φ) as discrete escin-rich solid domains (excluding the fluorescent dye) dispersed in a continuous DMPC-rich fluid phase (containing the RhPE dye). Only the fluid character of the liquid-ordered (L_O)-phase of the lipid bilayer enabled phase coexistence at equilibrium with the liquid-disordered (Lα)-phase into spherical GUVS (right panel). The bilayer $L\alpha-L_O$ coexistence appeared still fluid-like as far as the black domains appeared with the rounded boundaries continuing the liquid domains (see inset image). With intrinsic mixing of components in a broad range of escin concentrations (up to ca. 40% w/w), biphasic 2Φ-segregation was systematically observed in almost all GUVs present in the microscopy field (including encapsulated vesicles; see Figure 2A, bottom). However, no stable GUVs were obtained at higher escin concentrations (above 40% w/w), as expected for the solid-like membrane with a high fragility insufficient to cause GUV swelling. Therefore, our observations confirm the longitudinal integration of escin into DMPC to elicit a $1\Phi \rightarrow 2\Phi$ fluid phase segregation into escin-rich L_O-domains dispersed in the continuous DMPC-rich Lα-phase of the phospholipid bilayer (see schematic in Figure 2A; bottom).

3.2 Extrinsic escin insertion induces membrane stiffening following solid-like decoration in DMPC-based bilayer vesicles

When escin was externally incorporated into previously formed DMPC vesicles, as inserted from the outer medium, we defined it as a transverse insertion (*ad finem* method). Figure 2B shows the rationale designed for this purpose (extrinsic insertion). We first prepared pure DMPC GUVs at the Lα-phase (escin absent in the lipid formula). Subsequently, we added escin monomers dissolved sub-micellar in the vesicle outside (at 40 μM final concentration). The hybrid DMPC–escin GUVs were stable in escin suspension (as no escin micelles were present to dissolve the lipids from the GUV bilayers at $c \approx 0.1mM \ll CMC$) (De Groot et al., 2018). During adsorption interaction with the outer escin monomers, the hybrid 1Φ-GUVs initially remained in the disordered Lα-phase as no phase segregation was observed during the first stages of escin adsorption (Figure 2B; left panel). However, after 1 h of escin incubation, we observed that most GUVs lost circularity (e.g., polygonal profiles). The escin-modified DMPC GUVs progressively formed flat edges that suggested the solid nature of the escin out-layer (Kharbedia et al., 2021), although globally maintaining a disordered fluidity in the underlying DMPC bilayer (see Figure 2B; left). As additional evidence for such extrinsic interaction during the initial adsorption stage, the inner "matrioska" vesicles remained fluid-like with a rounded (flexible) aspect as staying protected to escin adsorption from the exterior (Figure 2B; bottom). In reaching adsorption equilibrium after incubation with escin for 24 h (Figure 2B; left panels), these vesicles undergo biphasic 2Φ-segregation. Over time, we observed an exclusion of the fluorescent probe from the blacked (escin-rich) areas where the flatter geometries suggested a solid-like character, the planar edges. However, the colored (DMPC-rich) areas remained fluid-like as evidenced by the fluorescent RhPE dye in the disordered Lα-phase, the rounded vertices (see schematics in Figure 2B; bottom).

The aforementioned empirical observations reveal how the transverse escin integration in DMPC membranes follows a two-stage adsorption–reorganization mechanism, as observed in other fluid membranes (Serrien et al., 1992; Muñoz et al., 2000; Langevin and Monroy, 2014). Firstly, escin adsorption induces extrinsic membrane stiffening in the flexible (Lα) DMPC membrane; primary relaxation. Once adsorbed, escin has enough time to reorganize and then equilibrate within the DMPC bilayer. Hence, the hybrid membrane undergoes phase segregation from 1Φ (Lα-phase) to 2Φ (phase demixing); secondary relaxation. The rigid escin-rich domains appear solid-like in the flattened vesicle edges, becoming mechanically equilibrated through flexible joints constituted by rounded DMPC-rich vertices constituted by the continuous Lα-phase (see schematics in Figure 2B; bottom). The rigid domains are presumably escin-rich because the fluorescent dye is excluded out from the laterally ordered hydrophobic arrangement constituted as lateral stacks between the steroidal moieties of the escin molecule (Sreij et al., 2017; Penfold et al., 2018). In agreement with previous hypotheses about structural condensation (Sreij et al., 2017; Geisler et al., 2019; Glickman et al., 2020), our results suggest reaching the equilibrium status of escin inside the phospholipid bilayer through the direct interaction between the acyl chain hydrophobic core of the membrane and the aglycone counterpart of the rigidizing molecule, similar to the structural compaction mediated by cholesterol between phospholipids and sphingolipids in real biomembranes (Van Meer et al., 2008; Espinosa et al., 2011).

3.3 Transverse escin penetration inducing crystallization in DMPC monolayers

To confirm the crystalline nature of the membrane escin-rich domains at low temperatures ($T = 4^{o}C \ll T_m$), we studied the transverse incorporation of escin in a simplified model based on Langmuir DMPC monolayers penetrated by the escin monomers from the subphase below (see Section 2). As an initial state of DMPC compaction, we considered the bilayer equivalent status compatible with the GUV state (corresponding to the lateral pressure $\pi = 30mN/m \approx \pi_b$) (Marsh, 1996). Figure 3A shows the formation of black domains (excluding the fluorescent dye) from the continuous fluid phase (including the dye within); they evolved in a nucleation process of crystal growth under constant area (see caption for details). Several days after monolayer formation, we observed the grown crystals as polygonal plates with sharp edges and a homogeneous size of ca. 2 μm (see Figure 3A; zoomed image of escin crystals). The observed escin crystals remained practically static for days, which suggested an equilibrated formation from a very dense phase, arguably a liquid condensed or an ordered fluid phase. The static character and highly conserved morphology of the crystalline textures agree with previous studies with monolayers of the Quillaja saponin (Böttcher and Drusch, 2017; Böttcher et al., 2017). The observed nucleation-growth sequence suggests a driving mechanism of surface reorganization with the monomers diffusing from the bulk solution (Figure 3B). This low-temperature incorporation-freezing mechanism could be dependent on the limited availability of adsorption sites in the preformed DMPC–escin monolayer (entropic adsorption) or, most probably, on the monolayer capacity to cohesively attract escin (enthalpic adhesion). We performed control experiments in the hybrid DMPC–escin monolayers discarding at high-temperature crystal formation ($T = 38oC \gg T_m$). No escin crystals were observed under the epifluorescence microscope (using RhPE dye as heterogeneity reporter) or under the BAM (Brewster microscopy does not need any dye to reveal inhomogeneities). An additional control ensures that the observed escin crystallization results from the presence of RhPE in the DMPC monolayer (its hydrophilic headgroup could induce freezing as nucleation seeds). No domains were observed by epifluorescence in the high-temperature escin–DMPC system (even in the presence of 10% w/w RhPE). These negative controls ruled out the possibility of structural artifacts that could complicate the interpretation of our dynamic results.

As a further insight going beyond the aforementioned qualitative analysis on low-temperature crystallization, we studied the transversally organized incorporation of escin by taking advantage of the dye-free visualization enabled under the BAM after DMPC monolayer formation in the homogenous L_O-state at low temperature ($T = 4oC \ll T_m$: see Figure 3C). Escin was injected

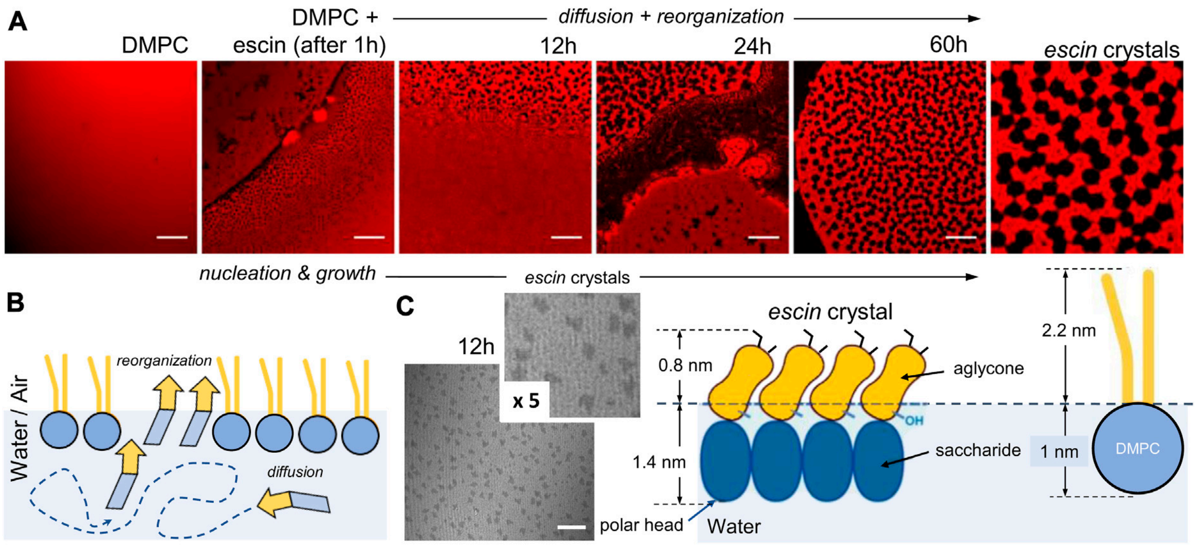

FIGURE 3
Crystal nucleation and growth process under escin insertion in Langmuir monolayers at low temperature ($T = 4°C \ll T_m$). **(A)** Epifluorescence microscopy shows the time evolution of the penetrating interaction of escin with a DMPC-monolayer fluorescently labeled with RhPE (0.1% mol). The DMPC-richer is the monolayer region, the brighter appeared in the red channel of rhodamine fluorescence emission (see Section 2, scale bars: 20 μm). The first microscopy snapshot corresponds to the bare DMPC monolayer [under bilayer-equivalent surface pressure $\pi_b \approx 30mN/m$]. Then, the escin surfactant is injected into the subphase (0.1 mM final), and the epifluorescence images are captured at different times over 3 days. A nucleation-growth process is recorded as small grains of ordered phase (escin-rich; black) appearing increasingly larger and darker with longer times over a brighter background corresponding to the disordered phase (DMPC-rich; white). (Right zoom) After 60 h of escin adsorption, the hybrid DMPC–escin monolayer reaches a steady appearance as escin crystals with a homogeneous size (ca. 2 μm) and a quite conserved polygonal morphology in equilibrium with the DMPC-rich phase (x5 zoom). However, no presence of domains or any other monolayer heterogeneity was observed by epifluorescence in the high-temperature system (homogeneous monolayer at $T = 38oC \gg T_m$). **(B)** Schematics of a possible escin adsorption scenario from the water subphase to the lipidic air–water (A–W) interface. The soluble surfactant (escin) diffuses from the bulk to the A–W interface. Here, escin penetrates and reorganizes to reach the equilibrium with the lipid component (DMPC). **(C)** Brewster angle microscopy (BAM) of the low-temperature DMPC monolayer penetrated by escin 12 h after injection in the subphase ($T = 4oC$; scale bar: 20 μm). The nucleation of monolayer escin crystals is evidenced by a thickness smaller (darker) than the DMPC-continuous phase (brighter). (Inset) The nascent crystals are quite heterogeneous in size (ca. 2 microns) at compatibility with the epifluorescence images (in A). No presence of domains or any other monolayer heterogeneity was observed by BAM in the high-temperature system (homogeneous monolayers at $T = 38oC \gg T_m$). Molecular modeling. The escin crystals are formed by quadrupolar amphiphilic interactions composed of hydrophobic stacking between the core rings in the aglycone moieties (longitudinal van der Waals forces) and hydrogen bonding between the saccharide heads dangling in water (transverse adsorption forces). This molecular model assumes a locally thinner monolayer at the level of the escin crystals than that in the thicker phase mainly composed of DMPC (see main text for structural determination).

into the subphase under the same aforementioned conditions, leading to the monolayers in Figure 3A (except for the absence of dye). After 12 h of incubation, the small solid domains started to nucleate at low temperatures (Figure 3C; 12 h panel). They appeared dark with an irregular sharp-edged texture, typical for nucleating crystals (see inset). The crystal size was similar to that observed in the presence of dye (see Figure 3A; panel for 12 h). However, in the control experiments performed at high temperatures ($T = 38°C \gg T_m$), BAM did not reveal domains of any kind (even in the presence of 10% w/w RhPE dye potentially acting as nucleation seed). To analyze these BAM experiments, we considered the different optical contrasts given by the respective refractive indices ($n_{PC} \approx 1.4$ for DMPC, and $n_{esc} \approx 1.8$ for escin; see Section 2). As regards the BAM images at low temperature ($T = 4\,°C \ll T_m$), we detected the escin crystals with an optical aspect significantly darker than that observed in the continuous phase (Figure 3C; inset), indicating a monolayer thickness larger in the continuous phase than for the dispersed crystals (see Drude's equation in Section 2). The average ratio of BAM reflectivity was experimentally measured with an over-unity value ($R_P^{(L)}/R_P^{(S)} = 1.45 \pm 0.12$), evidencing a fluid phospholipid monolayer thicker by the larger head-to-tail length than the thinner crystals (assumed to comprise smaller escin molecules; see schematics in Figure 3C). Regarding specific molecular dimensions in the monolayer arrangement (see Figure 3C; right panel), for DMPC, we expected a stretched molecular length, including the hydrated polar head $L_{PC} \approx 3.2\,nm$) (Van Meer et al., 2008; Philips et al., 2009). However, for escin, we expected a smaller length, which generalized structural X-ray and neutron scattering data $L_{esc} \approx 2.2\,nm$ (Sreij et al., 2019; Geisler et al., 2020a). From this plausible molecular modeling, we estimated the thickness ratio $(L_{PC}/L_{esc})^2 \approx 2.1$ in qualitative agreement with BAM measurements, that is, $(L_{PC}/L_{esc})^2 \cong (R_P^{(L)}/R_P^{(S)})(n_{esc}/n_{PC})^2 = 2.1 \pm 0.2$ by assuming $n_{esc}/n_{PC} = 1.20$.

3.4 Escin membrane insertion depending on the DMPC-monolayer packing status as determined by surface pressure and temperature

The aforementioned observations on escin crystal formation at low temperatures suggested a two-step mechanism mediated by

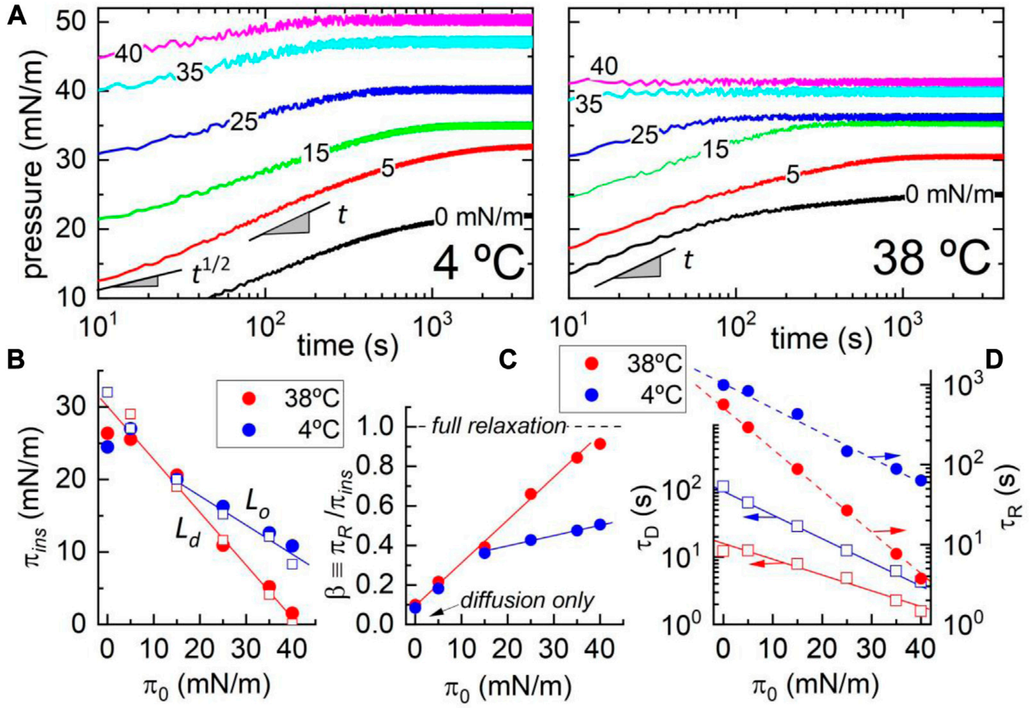

FIGURE 4
(A) Adsorption kinetics of escin on a DMPC monolayer at different initial states ($\pi(\pi_0; t)$ for π_0 = 0, 5, 15, 25, 35, and 40 mN/m). Escin is dissolved at a constant bulk concentration below the CMC (ca. 0.1 mM), and the system is considered at 4°C (left panel) and 38°C (right panel). The absolute surface pressure is tracked in triplicate, and the averaged kinetic plot is fitted to the BPGP equation (Eq. 1; see main text for details). The best fitting parameters plotted in the following panels are obtained from the observed adsorption kinetics, and the informed errors come from fitting to the averaged plots. **(B)** Equilibrium insertion pressure π_{ins} as a function of initial pressure π_0 upon escin incorporation into the DMPC monolayer. **(C)** Energy balance between the amplitude of internal reorganization and the insertion pressure at equilibrium as a function of initial pressure π_0. **(D)** Adsorption kinetic parameters: diffusion times τ_D (left axis) and membrane reorganization times τ_D (right axis) measured as a function of temperature and initial pressure π_0. The relative fitting errors are typically lower than 10% in the bottom graphs, thus compatible with the symbol size. Figure 4A shows the kinetic plots recorded in temperature regimes: low-T at which the phospholipids chains become tightly packed as mesogenically arranged in an ordered state (LO-phase at T 4 oC≪Tm; left panel); high-T at which DMPC chains are in a disordered state (LD-phase at T 38 oC≫Tm; right panel). The initial diffusion of escin is revealed slower at lower pressures, whereas the terminal escin incorporation is reached at higher pressures. Such kinetic bimodality becomes evenmore pronounced when the lipid packing and temperature are lower [Figure 4A; left panel]. This difference in incorporation is best evidenced when one analyzes the equilibrium insertion pressure as a function of initial pressure [see πins vs. π0 plots in Figure 4B]. Here, we clearly see that when the lipids are arranged in an expanded LD-phase, there is hardly any significant difference in escin incorporation between low and high temperatures. However, when the initial monolayer pressure is higher than π0 * ≈ 15mN/m (corresponding to the LD → LO transition), the equilibrium insertion pressure occurs higher in the LO-phase at a lower temperature. This effect is arguably caused by a reduced escin mobility in the more compacted phase, thus allowing an enhanced cohesive interaction (enthalpic adhesivity) rather than a mere passive steric hindering under adsorption.

initial nucleation and further growth. Figure 4 shows low-temperature biphasic kinetics driven by bulk-to-surface diffusive adsorption somewhat limited by a terminal reorganization process (Dukhin et al., 1994). Although similar adsorption kinetics occurs at higher temperatures, the surface system remains monophasic into a disordered fluid phase. In a previous study, we evidenced a preference for escin for heterogeneous demixing in DMPC monolayers at the lower temperatures studied (Sreij et al., 2017). In the current work, we further explored this phase-separation behavior in more detail, detecting the inductive role of ordered phospholipids in solid escin insertion into quasi-2D crystalline monolayers. The adsorption kinetics at the A–W interface was studied as a function of the packing state of the lipids on the supporting DMPC membrane. Specifically, we tracked surface pressure (π) for different penetration statuses at variable initial pressures (π_0) and temperatures (T). The system was considered for fixed (sub-micellar) escin concentration ($c = 0.1\,mM \approx 0.25\,CMC$) (Kharbedia et al., 2021).

Figure 4A shows the kinetic plots recorded in temperature regimes: low-T at which the phospholipids chains become tightly packed as mesogenically arranged in an ordered state (L$_O$-phase at $T = 4\,°C \ll T_m$; left panel); high-T at which DMPC chains are in a disordered state (L$_D$-phase at $T = 38\,°C \gg T_m$; right panel). The initial diffusion of escin is revealed slower at lower pressures, whereas the terminal escin incorporation is reached at higher pressures. Such kinetic bimodality becomes even more pronounced when the lipid packing and temperature are lower [Panel **(A)**; left panel]. This difference in incorporation is best evidenced when one analyzes the equilibrium insertion pressure as a function of initial pressure [see π_{ins} vs. π_0 plots in Panel **(B)**]. Here, we clearly see that when the lipids are arranged in an expanded L$_D$-phase, there is hardly any significant difference in escin incorporation between low and high temperatures. However, when the initial monolayer pressure is higher than $\pi_0^* \approx 15\,mN/m$ (corresponding to the L$_D$ → L$_O$ transition), the equilibrium insertion pressure occurs higher in the L$_O$-phase at a lower temperature. This effect is arguably caused by a reduced escin mobility in the more compacted phase, thus allowing an enhanced cohesive interaction (enthalpic adhesivity) rather than a mere passive steric hindering under adsorption.

3.5 Escin penetration process: adsorption follows membrane reorganization

3.5.1 Theoretical BPGP framework

According to the adsorption theory by Graham and Phillips (1979), substantiated by Pethica's problem for monolayer penetration (Pethica, 1955), and Buttler's theory for the thermodynamics of the surface of solutions (Buttler, 1932), the observable kinetics follows an adsorption–reorganization process, thereby a pressure penetration jump occurs with respect to the initial status $\pi(\pi_0, c) = \pi_0 + \pi_P(\pi_0, c)$ (see ref. Dukhin et al. (1994) for a comprehensive treatise). Hereinafter, this is called the Buttler–Pethica–Grahams–Phillips (BPGP) theory at a constant area, the BPGP kinetics holds (Graham and Phillips, 1979; Dukhin et al., 1994; Muñoz et al., 2000):

$$\pi_P(t; \pi_0, c) \approx \pi_{ins} - \left[(\pi_{ins} - \pi_R) e^{-\sqrt{t/\tau_D}} + \pi_R \right] e^{-t/\tau_R}, \qquad (1)$$

where $\pi_{ins}(\pi_0, c) = \int_{\pi_0}^{\pi} \Gamma_{esc}(\pi_0, c) d\mu_{esc}(c)$ is the equilibrium insertion pressure as determined by Gibbs' surface excess of escin concentration ($\Gamma_{esc} \equiv A_{esc}^{-1}$). This is given for the chemical potential of the surfactant molecule $\mu_{esc}(c) = \mu_{esc}^{(0)} + k_B T\, lnc$ (Buttler, 1932). Here, the relaxation pressure $\pi_R(\pi_0) \leq \pi_{ins}(c, \pi_0)$ accounts for the dissipative amount of surface energy due to internal reorganization.

This bimodal BPGP kinetics considers two consecutive steps (Buttler, 1932; Pethica, 1955; Graham and Phillips, 1979; Dukhin et al., 1994). First, the initial adhesive adsorption is characterized by the diffusive time $\tau_D(c, \pi_0)$, under the extrinsic degree of transverse diffusivity $\alpha(c, \pi_0) \equiv (\pi_{ins} - \pi_R)/\pi_{ins} = 1 - \pi_R/\pi_{ins}$. Second, a terminal relaxation upon cohesive escin penetration at a longer reorganization time $\tau_R(\pi_{ins}) \gg \tau_D(c, \pi_0)$, under an intrinsic degree of longitudinal relaxation $\beta(c, \pi_0) \equiv \pi_R/\pi_{ins}$ ($\alpha + \beta = 1$). For binary monolayers composed of the insoluble component (DMPC), as penetrated by the soluble surfactant (escin), the surface free energy holds a thermodynamical balance (Buttler, 1932; Pethica, 1955; Graham and Phillips, 1979; Dukhin et al., 1994; Fainerman and Vollhardt, 1999):

$$G(c, \pi_0) \Rightarrow \pi A = \pi_0 A_{PC} + \pi_{ins}(c, \pi_0) A_{esc} - E_{coh}(c, \pi_0), \qquad (2)$$

under cohesive energy $-E_{coh}(\pi, c)/k_B T = \omega(c)(\pi - \pi_0)/\pi_0$, which is determined by the penetrating molecules occupying the relative partial area $\omega(c) \equiv A_{esc}/A_{PC} = (A - A_{PC})/A_{PC}$ (defined at fixed bulk concentration c), as in the well-known Buttler's equation (Buttler, 1932; Dukhin et al., 1994). The bare BPGP cohesivity is defined in the ideal limit of maximal insertion (i.e., $-E_{coh}(\pi, c)/k_B T \to \omega(c)$ at $\pi^{(0)} = \pi_{ins}(\pi_0 \to 0)$; see Figure 3B). Only for the bare lipid monolayer, we expect a null cohesivity (i.e., if $\omega = 0$ at $A(c = 0) = A_{PC}$, then $E_{coh}(\pi, c = 0) = 0$). At thermodynamic equilibrium $dG(c, \pi_0) = d(\pi A) = 0$, a cohesive trade-off is expected under initial pressure (π_0) (Buttler, 1932; Pethica, 1955; Graham and Phillips, 1979; Dukhin et al., 1994; Fainerman and Vollhardt, 1999):

$$\begin{aligned} \Delta E_{coh}(c, \pi_0) &\approx \left[\Delta E_{\parallel}(c, \pi_0) + \Delta E_{\perp}(c, \pi_0) \right] \\ &= \pi_0 \delta A_{PC}(c) + \pi_{ins}(c, \pi_0) \delta A_{esc}(c), \end{aligned} \qquad (3)$$

corresponding to escin and DMPC interacting with each other under condensing partial areas, that is, $\delta A_i = A_i^{(initial)} - A_i^{(final)} > 0$ (for $i = \{PC, esc\}$). Hence, the area contractions appear from the cohesive interactions, adsorption attractions at enhancing transverse adhesion (this is an extrinsic cohesion, i.e., $-\Delta E_{\perp}(c) \approx E_{ads} > 0$) and area compaction at hindering longitudinal compressibility (this is an intrinsic cohesion, i.e., $-\Delta E_{\parallel}(c) \approx K > 0$).

Therefore, the constitutive BPGP parameters depend on the initial pressure (π_0), which makes the insertion pressure decrease conversely, that is, $\pi_{ins} = \pi_{ins}^{(0)} - \alpha \pi_0$ (by defining $\pi_{ins}^{(0)} \equiv -\Delta E_{coh}/\delta A_{esc}$ and $\alpha \equiv \delta A_{PC}/\delta A_{esc}$ in Eq. (3)). This effectively linear relationship defines a positive intercept essentially due to cohesive energy, that is, $\pi^{(0)} \gg 0$, and a near unity negative slope given by the structural compaction ratio, that is, $\alpha \approx 1$ (for $\omega^{-1} = A_{PC}/A_{esc} \approx 1$), as empirically evidenced (see Figure 4B). As a consequence of structural cohesion, the higher relaxation strength is enabled at lower insertion pressures, that is, $\beta \equiv \pi_R/\pi_{ins}$ ($\sim \pi_0/\pi_{ins}$; see Figure 4C). In mechanical terms, the equilibrium pressure leads to higher membrane rigidness under lower initial ordering imposed by DMPC but to higher ordering scaffolded by inserted escin [see Eq. (2)]. Consequently, we expect the surface stiffness to vary under uniaxial deformations by the respective molecular compactions δA_{PC} and δA_{esc} (Catapano et al., 2011; López-Montero et al., 2013; Langevin and Monroy, 2014). As coupled in series ($\delta A = \delta A_{PC} + \delta A_{esc}$), the surface rigidness per molecule stems from the total surface interaction considered homogeneous as $K\, dA \Leftarrow A\, d\pi$; $K = K_{PC} + K_{esc}$ is an effective bulk modulus for membrane dilatation (Arriaga et al., 2010b) (see Section 3.6). Furthermore, the effective adsorption rates are mechanically evaluated as a sequence of insertion and reorganization events (i.e., $\tau_{ads}^{-1}(c, \pi_0) = \tau_{ins}^{-1}(1 + \tau_{ins}^2/\tau_R^2) = \tau_D^{-1} + 2\tau_R^{-1}$).

3.5.2 Dynamic regimes

From the adsorption kinetics observed in the experiments (see Figure 4), two different regimes can thus be inferred as limiting dynamic behaviors:

A) Diffusion controlled at short insertion times (i.e., $\tau_D \approx \tau_{ins} \ll \tau_R$, thus $\tau_{ads} \approx \tau_D$). In this slow relaxation, the BPGP regime ($\tau_R \gg \tau_D$), the initially quick insertion time is controlled by the faster diffusional adsorption (i.e., $\tau_{ins} \approx \tau_D$) (Monroy et al., 1998; Díez-Pascual et al., 2007), which is accelerated by the adhesion energy ($-E_{ads} \gg 0$). The penetration pressure is hence dominated by the insertion pressure as $\pi_P^{(D)}(t) \approx (\pi_{ins} - \pi_R)[1 - e^{-\sqrt{t/\tau_D}}]$ (for $\pi_{ins} \gg \pi_R$). This diffusion-controlled regime is discerned as $\pi_P^{(D)}(t \to 0) \sim t^{1/2}$ (see Figure 4A; left panel), which corresponds to low temperature and low initial pressure, allowing for transverse escin insertion (for $\pi_0 \ll \pi_{ins}$; Figure 4B). The constitutive relationships in Eqs 2,3 imply a bulk-to-surface diffusivity controlled by an adsorption potential of cohesive energy susceptible to declining with decreasing availability of surface-free sites for escin cohesivity (i.e., $E_{ads} \to 0$ for $A \to A_{PC}$ at $\pi_{ins} \to 0$). In other words, adsorption energy becomes strongly attractive under

TABLE 1 Energetic surface compaction parameters for the DMPC–escin system (as determined from the experimental data in Figure 3B). The structural parameters for the corresponding cross-sectional areas are taken from literature data (as in Section 3.3) (for DMPC: Van Meer et al., 2008; Philips et al., 2009; for escin: Sreij et al., 2017; Geisler et al., 2020a).

Surface phase	$\pi_{ins}^{(0)}$ (mN/m)	$\alpha \equiv \delta A_{PC}/\delta A_{esc}$	A_{PC} (nm^2)	A_{esc} (nm^2)	$-E_{ads} \approx \pi_{ins}^{(0)} A_{esc}$
Liquid-disordered	30 ± 1	0.75 ± 0.12	≈ 1.0	≈ 4.4	$33\,k_B T$
Liquid-ordered	24 ± 2	0.56 ± 0.15	≈ 0.5	≈ 0.9	$5k_B T$

transverse escin penetration, similar to the adhesive case in the classical BET adsorption theory (Brunauer et al., 1938). Otherwise, surface adhesion by inserted escin facilitates adsorption from the bulk phase into the DMPC-based surface, that is, $-E_{ads} \approx \omega\pi_{ins}A_{PC} \approx \pi_{ins}^{(0)}A_{esc} \gg 0 \Rightarrow E_{ads} \approx -\Delta E_{\perp}(\pi_0) \approx -\alpha\pi_0\delta A_{esc}$ (for $\pi_{ins} \gg \pi_0$ and $\delta A_{esc} > 0$). The initial adsorption times are observed to be effectively accelerated due to a cohesively improved escin insertion in an attractive adsorption potential well, that is, $\tau_D(\pi_0) \approx \tau_D^{(0)} exp(-\Delta E_{\perp}/k_B T)$ (Brunauer et al., 1938) (see experimental data in Figure 4D). Upon adhesive attraction leading to escin compaction ($\delta A_{esc} > 0$), this transverse energy is calculated as $\Delta E_{\perp} = \pi_0\delta A_{esc} \gg 0$ (for $\pi_0 \ll \pi_{ins}$). Hence, the transverse adhesive adsorption is expected to become faster with increasing lateral compaction (raising π_0).

B) Insertion controlled under internal reorganization (i.e., $\tau_R \ll \tau_D \approx \tau_{ins}$, thus $\tau_{ads} \approx \tau_R/2$). In this terminal BPGP relaxation regime ($\tau_R \ll \tau_D$), the penetration pressure increases as $\pi_P^{(R)}(t) \approx \pi_{ins}[1 - e^{-t/\tau_R}]$ (for $\pi_{ins} \approx \pi_R$), which is controlled by the global cohesive energy that retains the membrane internally compacted ($E_{coh} \gg E_{ads}$). Terminal insertion follows first-order kinetics with an insertion time expected to be nearly twice the internal reorganization time ($\tau_{ins} \approx 2\tau_R$). The reorganization-controlled regime varies linearly with time as $\pi_P^{(R)}(t \to 0) \sim t$ (Figure 4A; right panel), being predominant at high temperatures and relatively high pressures dominated by longitudinal escin compaction (for $\pi_0 \gg \pi_{ins}$; Figure 4B). The terminal relaxation is expected as a lateral reorganization of the inserted escin in the monolayer, which is further compacted. Consequently, longitudinal in-plane compaction energy globally favors the insertion of escin at approximate dependence on the pre-existing longitudinal packing for DMPC, that is $-\Delta E_{coh} \Rightarrow \Delta E_{\parallel} \approx \pi_0\delta A_{PC}$ (for $\pi_0 \gg \pi_{ins} \to 0$). Hence, a first-order reorganization kinetics appears within the DMPC-supporting structure under empirical Debye-like relaxation times, $\tau_R(\pi_0) \approx \tau_R^{(0)} exp(-\Delta E_{\parallel}/k_B T)$ (Hill and Dissado, 1985) (see data in Figure 4D). Based on effective cohesive attraction leading to more compact phospholipids ($\delta A_{PC} > 0$), such longitudinal energy is calculated as $\Delta E_{\parallel} = \pi_0\delta A_{PC} \gg 0$ (for $\pi_0 \gg \pi_{ins}$). Hence, longitudinal reorganization is expected to become faster with increasing lateral compaction (increasing π_0).

For adequate parametrization of the adsorption process, the experimental results in Figure 4 demonstrate the two sequential regimes predicted by the BPGP theory (also inferred from the qualitative analyses of the microscopic membrane textures in Figures 2, 3): 1) initial extrinsic incorporation of escin toward the bulk vicinity of the adsorbent monolayer and 2) subsequent intrinsic penetration of escin into the phospholipid monolayer. We further analyze the corresponding energetics and relaxation times as determined from the initial monolayer pressure in differential DMPC compaction statuses determined by temperature.

3.5.3 Adsorption energetics

The equilibrium pressures in Figure 4B demonstrate the energy trade-off predicted between the final escin insertion and the initial DMPC state [see Eq. (2)]. For constant escin concentration, we detect in both phases the linear relationship $\pi_{ins}(\pi_0) = \pi_{ins}^{(0)} - \alpha\pi_0$. The positive intercept indicates cohesive adsorption dominance by inserted escin ($\pi_{ins}^{(0)} \equiv -E_{ads}/A_{esc} \gg 0$). The negative slope indicates higher escin compaction as referred to the saturated DMPC phospholipid ($\alpha \equiv \delta A_{PC}/\delta A_{esc} < 1$ i.e., $\delta A_{esc} > \delta A_{PC}$). The best-fitted values obtained for these parameters are shown in Table 1 in reference to the different L_D/L_O states of structural compaction.

At structural compatibility with the high- and low-temperature states of DMPC (liquid-disordered $\mathrm{L_D}$/liquid-ordered $\mathrm{L_O}$), we detected differences determined by the molecular malleability of the reconfigurable escin (see schematics in Figure 3). The observed compaction changes are larger in the fluid-like $\mathrm{L_D}$-phase than in the solid-like $\mathrm{L_O}$-phase (Geisler et al., 2020a). Specifically, we found $\pi_{ins}^{(0)}(D) \gg \pi_{ins}^{(0)}(O)$ for initial pressures and $\alpha_D > \alpha_O$ for compaction slopes. By assuming the structural data reported in Table 1, we estimated $\delta A_{PC} \approx 0.5\,nm^2$ and $\delta A_{esc} \approx 3.6\,nm^2 \gg \delta A_{PC}$, in qualitative agreement with the values found for the compaction ratio (see values for α in Table 1). Furthermore, we estimated the adsorption energy for escin into the DMPC monolayer, that is, the adhesive potential well ($E_{ads} \approx \pi_{ins}^{(0)}A_{esc}$). This interaction energy was quite high in the $\mathrm{L_D}$-phase at high temperature ($-E_{int} \approx -E_{ads}^{(D)} \approx 33k_B T$), whereas it was much lower in the ordered $\mathrm{L_O}$-phase, with less interaction at lower temperatures ($-E_{ads}^{(O)} \approx 5k_B T \ll -E_{ads}^{(D)}$). Figure 4B demonstrates the more facilitated escin insertion under conditions of higher surface disorder, high temperatures (higher adsorption availability for escin), or both. Figure 4C shows the difference in the relaxation amplitudes for escin reorganization $\beta(\pi_0) \equiv \pi_R/\pi_{ins}$. Although the relaxation strength increases linearly with the initial DMPC pressures (π_0), they experience a clear breakdown across the $\mathrm{L_D} \to \mathrm{L_O}$ transition.

According to the adsorption BPGP kinetics, the values measured for $\beta(\pi_0)$ reveal empirically the strenght of the subsidiary reorganization compared to the initial diffusive transport at dependence of the membrane coverage status (see Eq. 1). At low surface coverage (i.e., at $\pi_0 \approx 0$), escin insertion is chiefly governed by extrinsic diffusion (then $\pi_{ins} \approx \pi_P^{(D)}(t \to \infty) \gg \pi_R$; thus, $\beta \approx 0$). However, in highly covered surfaces (i.e., at $\pi_0 \to \pi_b \approx 30mN/m$), escin insertion is mostly dominated by intrinsic reorganization (then

TABLE 2 Experimental kinetic parameters for the DMPC–escin system in the high- and low-temperature states (as determined from the experimental data in Figure 3D). The estimated interaction energies are determined as per molecule.

Surface state	$\tau_R^{(0)}$ (s)	δA_{PC} (nm^2)	$-\Delta E_\parallel$	$\tau_D^{(0)}$ (s)	δA_{esc} (nm^2)	$-\Delta E_\perp$
High temperature	550 ± 25	0.4 ± 0.2	$\approx 20k_BT$	18 ± 1	0.3 ± 0.2	$\approx 12k_BT$
Low temperature	1020 ± 50	0.3 ± 0.2	$\approx 12k_BT$	120 ± 5	0.3 ± 0.2	$\approx 12k_BT$

$\pi_{ins} \approx \pi_P^{(R)}(t \rightarrow \infty) \approx \pi_R$, thus $\beta \approx 1$). As revealed by the kinetic plots in the panels of Figure 4A and the corresponding relaxation amplitudes in Figure 4C, the process is energetically free-diffusive only under limiting conditions for the practical absence of lipid at the interface (at $\pi_0 \rightarrow 0$). In the expanded disordered status, a progressive reorganization takes place independently of the initial pressure (at $\pi < \pi_0^* \approx 15mN/m$). However, a tipping point is detected near the $L_D \rightarrow L_O$ transition (as the onset of ordering for enhanced escin compaction in the L_O-phase of the phospholipid ca. $\pi_0^* \approx 15mN/m$). The phase coexistence emerges as the lipid concentration increases upward the tipping point (at $\pi > \pi_0^* \approx 15mN/m$ for $T \leq T_m \approx 23oC$). In these biphasic L_O/L_D states, the second reorganizational process becomes the most important in the lipid-covered surface (in approaching $\pi \rightarrow \pi_b \approx 30mN/m$). At lower temperatures ($T \ll T_m$), the membrane organization is hence controlled by the extrinsic diffusivity of the escin molecules toward the interface plane (in the L_D-phase at low insertion pressures $\pi_{ins} \ll \pi_0^*$) or by their intrinsic reorganization inside the membrane (in the L_O-phase at high insertion pressures $\pi_{ins} \gg \pi_0^*$). However, at high temperatures ($T \gg T_m$), the most relevant from a biological point of view, the subsidiary process for escin insertion leads to a dominantly intrinsic reorganization. We consider this relevant state to be closely corresponding to the liquid crystalline ordering of the fluid lipid bilayer at nearly physiological temperatures (Evans and Hochmuth, 1976; Philips et al., 2009; Espinosa et al., 2011). By referring to the ordered molecular packing in DMPC monolayers (L_O-phase), this reference bilayer-like state corresponds to high temperature ($T_{high} = 38oC \gg T_m$) and high pressure ($\pi_b \approx 30mN/m \gg \pi_0^*$) (Marsh, 1996). These biomimetic conditions correspond to an average surface area $A_{PC} \Rightarrow A(L_O) \approx 0.5\,nm^2$ (see Table 1), close to the molecular cross-section of a single phospholipid molecule in the L_O-phase (Evans and Hochmuth, 1976; Finegold, 1992; Marsh, 1996; Philips et al., 2009; Espinosa et al., 2011).

3.5.4 Adsorption kinetics

The kinetic data in Figure 4D show the escin-specific relaxation times as experimentally derived from the BPGP kinetics in Eq. 1: $\tau_D(\pi_0)$ for the initially faster membrane-extrinsic diffusion (left axis) and $\tau_R(\pi_0)$ for the subsidiarily slower membrane-intrinsic rearrangements (right axis). The best-fitting parameters that appeared as condensing partial areas together with associated energies are shown in Table 2 in reference to high- and low-temperature conditions of the cohesive reorganization.

The characteristic relaxations were faster with increasing temperature (T) and the initial monolayer pressure imposed by DMPC (π_0). At low temperatures ($T = 4o\,C \ll T_m$), the two adsorption times decreased exponentially (with increasing π_0), thus indicating a higher surface adhesivity with increasing membrane compaction (Figure 4D; blue symbols). At high temperatures ($T = 38\,oC \gg T_m$), the two characteristic escin insertion times also decreased exponentially. However, as evidenced by the higher decaying slope, the reorganization time displayed a marked tendency to decrease further at higher temperatures (Figure 4D; red symbols). Because the terminal reorganization is kinetically governed by in-plane transport (i.e., $\tau_R(\pi_0) \approx \tau_R^{(0)} exp(-\Delta E_\parallel / k_BT)$, under lateral interaction energy $\Delta E_{int} \Rightarrow \Delta E_\parallel \approx \pi_0 \delta A_{PC}$), we measured the faster reorganization times due to the much stronger compaction. The high-temperature behavior is clearly induced by cohesive escin at relatively low insertion pressure on the highly disordered (very expanded) L_D-phase of DMPC (i.e., $\delta A_{PC}^{(D)} \approx 0.5\,nm^2$ for $\pi_{ins} \ll \pi_0^* \approx 15mN/m$).

Comparing the reorganization times calculated with regard to the BPGP theory, we found the longest ones for the lowest temperature corresponding to the most escin-inserted states (escin-rich L_O-phase; i.e., $\tau_R(O) \gg \tau_R(D)$), corresponding to the most cohesive compactions induced by escin on the disordered phase of DMPC. For the extrapolated reference state of no escin insertion ($\pi_{ins} \rightarrow 0\,mN/m$), corresponding to the bare DMPC molecules in the closest-packed configuration (at $\pi_0 \rightarrow 40mN/m \gg \pi_b$), we roughly estimated the lateral compaction parameter in agreement with structural expectations (i.e., $\delta A_{PC}^{(D)} \gg \delta A_{PC}^{(O)}$). The energy for lateral reorganization was estimated to be higher in the more malleable disordered phase ($-\Delta E_{int}^{(D)} \approx 20k_BT$) than in the liquid-ordered status, in which it appeared as a cohesive energy for in-plane compaction ($-\Delta E_{int}^{(O)} \approx 12k_BT \Rightarrow \Delta E_\parallel$; see Table 2). Despite the longitudinal reorganizational differences found upon escin insertion, the faster diffusional times showed differences dictated by the transverse transport from the subphase toward an adhesive BET surface (Brunauer et al., 1938), that is, $\tau_D(\pi_0) \approx \tau_D^{(0)} exp(-E_{ads}/k_BT)$, under effectively adhesive adsorption energy (i.e., $E_{ads} > 0$) (Brunauer et al., 1938). Adhesion-activated adsorption is essentially determined by the capacity of escin to the compact area if cohesively adhered to the interface, that is, $\Delta E_\perp \approx -\pi_0 \delta A_{esc}$ (for $\delta A_{esc} > 0$). In experimental terms, we observed nearly the same compaction independently of temperature (see Figure 4D; left axis). This is compatible with the compaction parameter measured for escin in the two temperature conditions $\delta A_{esc}^{(high)} = \delta A_{esc}^{(low)} = 0.3 \pm 0.1 nm^2$ (see Table 2). By assuming the maximal structural compaction estimated earlier for the membrane components (i.e., $\delta A_{esc} \approx \delta A_{PC} \approx 0.3\,nm^2$), we calculated the transverse interaction parameter as a transverse adhesion energy of the same order as the lateral cohesion energy. For the closest-packed state ($\pi_0 = 40\,mN/m$), these are $\Delta E_\perp \approx \Delta E_\parallel \approx 12\,k_BT$. The neatly attractive (cohesive) behavior evidences the surface adsorption of escin as an activated process of surface cohesion essentially governed by the adsorption-enhanced diffusive transport from the bulk solution toward the

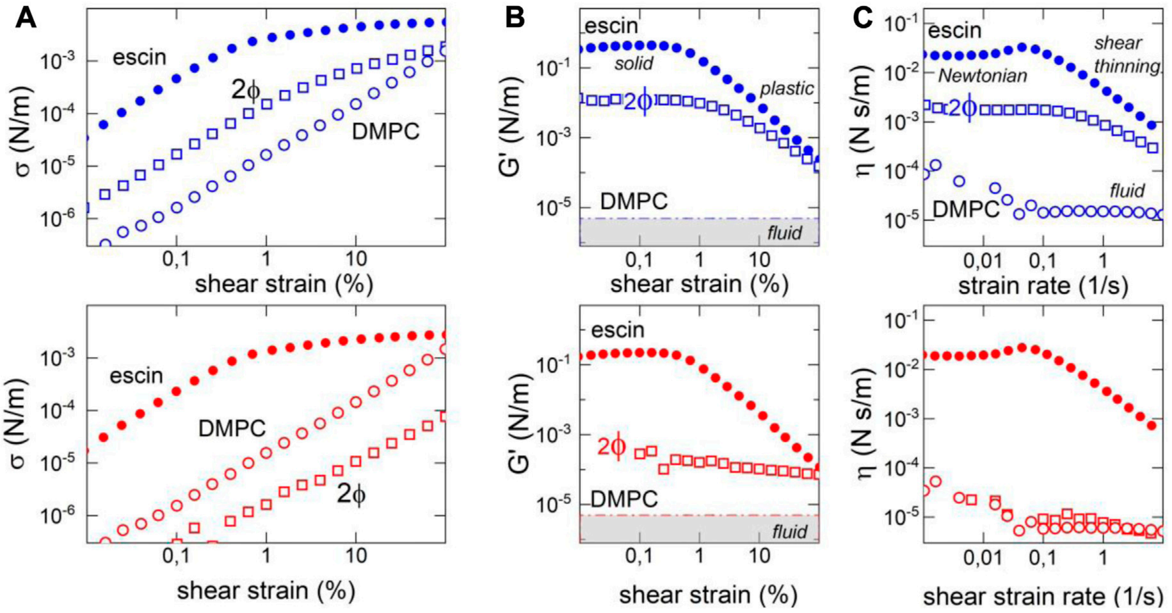

FIGURE 5
Surface shear rheology of escin–DMPC monolayers (at the biological reference status $\pi_b = 30mN/m$; measurements performed in triplicate; standard deviation 10% typically compatible with the dot size). The average data compared the low-temperature condition at $T = 4\,oC$ (upper panels; blue symbols) and the high-temperature condition at $T = 38\,oC$ (lower panels; red symbols). We show comparative graphs of pure escin (monophasic 1ϕ), pure DMPC (1ϕ), and escin interacting with DMPC as penetrating at a high degree of extrinsic insertion from the aqueous subphase at concentration 0.1 mM (biphasic 2ϕ). **(A)** Stress–strain plot at 1 Hz. **(B)** Shear rigidity modulus as a function of shear strain. **(C)** Dynamic shear viscosity as a function of shear strain rate. The bare escin monolayer behaves like a solid, whereas the DMPC monolayer is typically fluid. The mechanical interaction of both components in the escin-penetrated monolayer upon shear depends on the temperature. At low temperatures (4°C), they behave like a soft solid. However, at high temperatures (38°C), they do like a viscous fluid.

adhesive surface. As a matter of theoretical conjecture inferred from the aforementioned experimental observations, the amphipathic molecule β-escin should be highly surface active and self-adhesive, promoting membrane rigidness under the high lateral cohesion due to π–π interactions largely enhanced with increasing packing.

3.6 Mechanical impact of escin rigidness on Langmuir monolayers

The solid-like behavior of the bare escin molecule has been well-established in previous studies on Langmuir monolayers and bilayer vesicles of the pure component (Sreij et al., 2017; Sreij et al., 2019; Geisler et al., 2020a). However, little is known about its mechanical impact as imparting rigidity in phospholipid membranes, particularly in the biologically relevant packing status (i.e., the hypothetical liquid-ordered phase compatible with the bilayer packing) (Marsh, 1996). In a recent study on membrane mechanics using NSE with LUVs, we reported the impact of the escin–DMPC molecular interaction on the bending stiffness of highly curved bilayer membranes (Sreij et al., 2018). From the analysis of the NSE relaxation times performed at the molecular scale, we inferred an escin-dependent membrane stiffening as imparted on the fluid phase well above the melting transition of DMPC ($T \gg T_m = 23.6$℃). Here, we reported a deeper rheological assessment of the flat membrane configuration in the temperature regimes considered for the bilayer-equivalent state ($\pi_b \approx 30mN/m$) (Marsh, 1996). Under these conditions, the hybrid escin–DMPC system was organized as parallel plates of finite thickness under cohesive interaction with the penetrating escin (see Section 3.3; Figure 3). We measured the rheological response to planar shear corresponding to in-plane reorganizations of the membrane molecules and the out-of-plane relocation of escin produced under surface deformation (see Sections 2.4, 2.5).

3.6.1 Hookean regime: interaction energies

Figure 5 shows the two rheological scenarios explored at low temperatures (solid-like: blue symbols and upper panels) and high physiological-like temperatures (fluid-like: red symbols and lower panels). For the highly rigid escin monolayers, the stress-strain plots exhibit nonlinear softening above a yield point detected at very small strains (about $\gamma \approx 1\%$; see Figure 5A). The solid-like character of the monophasic escin monolayers is demonstrated as an extremely high value of the linear rigidity modulus detected at both temperatures ($G_0' \gtrsim 200\,mN/m$; Figure 5B). Such high values of shear rigidness actually correspond to the strong lateral cohesion energy, as inferred previously from the surface adsorption energetics (see Section 3.4). In effect, effective changes in rigidness are expected, describing the internal membrane cohesion as the elasticity coupling between the two orthogonal uniaxial deformations: the transverse surface insertion of escin and its longitudinal

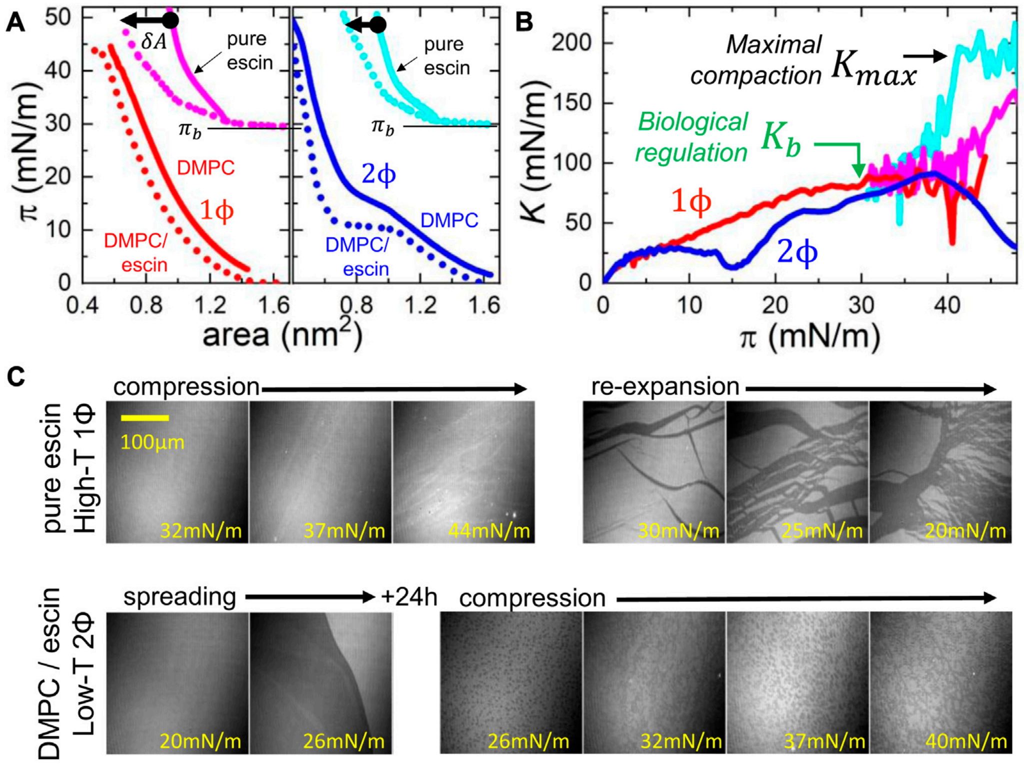

FIGURE 6
Experimental isotherms for hydrostatic compression of escin–DMPC monolayers. **(A)** Hydrostatic $\pi - A$ plots recorded under continuous compression at different temperature conditions. High-temperature monophasic (T = 38oC; left panel, reddish symbols). Low-temperature biphasic (T = 4oC; blueish symbols, right panel). (Legend) Compression from the low-pressure status (bottom isotherms): pure DMPC (straight lines); DMPC–escin mixture (30% w/w) (dotted lines). Compression from an initially adsorbed escin state (at $\pi_b \approx 30mN/m$; top isotherms): pure escin (straight lines); DMPC spread on escin solution (0.1 mM) (dotted line). The experiments were performed in triplicate, with the replicas reproducible within the experimental uncertainty (±1 mN/m for surface pressure and ± 0.15 nm^2 for molecular areas). The pure escin monolayers were extremely brittle under compression, thus being more variable ($\pi \pm 2$ mN/m and $A \pm 0.2$ nm^2). **(B)** Hydrostatic compression modulus (i.e., $K = -A\,(\partial\pi/\partial A)_T$ calculated as the numerical derivative of the smoothed isotherms). High-temperature monophasic states: liquid-disordered DMPC (1ϕ/L$_D$; red straight line); pure escin (1ϕ for solid-like in magenta). Low-temperature biphasic states: DMPC (2ϕ for L$_O$/L$_D$ coexistence in blue); pure escin (2ϕ solid crystals/L$_O$ in cyan). Two particular states of biological significance for escin insertion are tagged (corresponding to the high-temperature status): Maximal escin compaction ($K_{max} \approx 200mN/m$ at $\pi \approx 40 - 50mN/m$) and bilayer-equivalent state of biological regulation [$K_b \approx 70mN/m$ at $\pi_b \approx 30mN/m$]. **(C)** Monolayer morphologies as determined by BAM under hydrostatic compression (surface pressures indicated in yellow): (Upper filmstrip) Solid-like monolayers of pure escin under compression at high temperatures before collapse ($\pi_{col} \approx 50\,mN/m$); the further re-expansion fractures the solid plates that compose the uniform escin monolayer. (Lower filmstrip) Phase-separated monolayers of DMPC spread at high temperatures on a sub-micellar escin solution (0.1 mM). The monolayers were left overnight to keep reaching the adsorption equilibrium. After 24 h, they exhibit the escin-rich crystallite domains already shown rafting the liquid-disordered DMPC phase (see Figure 3). The resulting biphasic monolayers were BAM-monitored under uniform compression from the initial insertion pressure till collapse. The bi-phasic mesoscopic superstructure remains progressively crowded as an interacting network of discretely percolated domains composed of the rigid escin (dark domains of aglycone compacted moieties shorter than DMPC), as floating in the continuous phase of the molten phospholipid (appearing brighter corresponding to tailed molecules longer than escin).

reorganization (Espinosa et al., 2011). Consequently, the effective shear rigidity must be observed as an apparent surface modulus arising from the membrane cohesion as defined per molecular area, $E_{coh}\,(= E_{int} + \Delta E_{\parallel} + \Delta E_{\perp})/A \approx (1+\nu)G_0'$ (ν is the Poisson ratio) (López-Montero et al., 2013; see Section 3.5). For pure escin monolayers, we assumed $A_{esc} \approx 0.9\,nm^2$ and $E_{int} \approx 35k_BT$ (see Table 1), and $\Delta E_{\parallel} + \Delta E_{\perp} \approx 24k_BT$ (see Table 2), so that we can estimate the surface rigidness as an effective elasticity modulus for the solid-like status (i.e., $E_{coh} = (1+\nu)G_0' \approx 260\,mN/m$); in qualitative agreement with the experimental measurements of the shear modulus ($G_0' \gtrsim 200\,mN/m$; see Figure 5B). Hence, the Poisson ratio is estimated for these bare escin monolayers at $\nu \lesssim 0.2$, which is compatible with extremely high rigidity (Catapano et al., 2011; López-Montero et al., 2013). The solid-like character of these adsorption monolayers of water-soluble escin was further evidenced with respect to the fluid-like behavior of the Langmuir monolayers of the water-insoluble DMPC phospholipid (with apparent values of shear rigidity below the experimental uncertainty; see Figure 5B).

3.7 Hydrostatic compression: membrane dilatability and interdomain interaction

3.7.1 Hydrostatic compression isotherm and compression modulus: microscopic dilatability

In addition to the surface shearing experiments in the linear regime, we performed mechanical experiments probing the compression isotherms and the linear compression modulus of the DMPC monolayers spread over an escin-containing subphase (Catapano et al., 2011). Figure 6 shows measurements performed in the physiologically relevant states of escin–DMPC interaction at high temperatures compatible with the liquid-disordered molecular status of the phospholipid that always appeared monophasic as per entropic dominance. These high-temperature biomimetic systems were compared with the respective enthalpic statuses of high compaction compatible with escin adhesivity that appeared either monophasic for pure escin or biphasic after the mixing interaction with the liquid-ordered phase of DMPC (at low temperatures). The compression isotherms plotted in Figure 6A reveal a high-temperature dataset with an expanded-like monophasic behavior (left panel), contrasting the highly ordered condensed-like character of the biphasic statuses recorded at low temperature (right panel). On the one hand, high-temperature conditions impose the surface pressure to monotonically increase without strong structural change from the initial state up to collapse ($T = 38\,\mathrm{oC}$; Figure 6A; left). Even for the hybrid DMPC monolayers penetrated by escin at high pressure ($\pi_0 \rightarrow \pi_b = 30 mN/m$), the high cohesive compaction imposes a pressure renormalization under escin adsorption from expanded-like behavior at large areas to highly condensed statuses at smaller areas (i.e., a dominant cohesive term emerges in the fluid phase as $-E_{ads} = \pi_0 (A - A_{PC}) \approx \pi_0 \delta A$ characterized by a high partial area condensation $\delta A \approx 0.4\, nm^2$; see Figure 6A; left panel, and Table 2). On the other hand, low-temperature conditions strongly impact the biphasic $\mathrm{L_D}$–$\mathrm{L_O}$ behavior of the lipid DMPC monolayer. In particular, a broader and flatter coexistence region was observed for the hybrid DMPC–escin system ($T = 4\,\mathrm{oC}$; Figure 6A; right). However, weaker condensation statuses were observed under escin adsorption in the condensed DMPC monolayer previously formed in the $\mathrm{L_O}$-phase (in this case, $\delta A \approx 0.3 - 0.2\, nm^2$; see also Table 2). Under that low-temperature condition, cohesive interactions appear energetically more favorable when lateral contacts between DMPC and escin are intrinsically favored at high insertion status (see Figure 4B and Table 1; Section 3.5).

Figure 6B shows the calculated values of the hydrostatic compression modulus $K = -A (\partial \pi / \partial A)$, which describes the surface response to uniform changes in lateral pressure (Catapano et al., 2011; López-Montero et al., 2013). Interestingly, the nearly conserved bulk modulus of the hybrid DMPC–escin monolayers exhibits a "regulatory" plateau at the bilayer-equivalent packing pressure (π_b), that is, $K_b \approx 70 mN/m$ at $\pi_b \approx 30 mN/m$ (see caption for details). At higher compacting pressure ($\pi > \pi_b$), however, the modulus of lateral compressibility experiences further increases, especially for the very compact systems barely composed of pure escin and mixed with the liquid ordered phase of DMPC. The maximal compression modulus is identified in the pure escin monolayers $K_b \ll K_{max} \lesssim 200 mN/m$ at $\pi_{max} \gtrsim 40 mN/m$ (corresponding to $\pi_{ins} \rightarrow 0$, the reference state adopted for estimating the energies in Tables 1, 2; Section 3.5; see also Figure 3). We estimate the cohesion energy of escin under barely adsorption as $-E_{ads}^{(esc)} = K_{max} A_{esc} \approx 45\, k_B T$, clearly exceeding the longitudinal interaction energy identified for area reorganization, (i.e., $E_{coh} \gg \Delta E_{\perp}$) (see Table 2). Therefore, the effective compression modulus plotted in Figure 5B must be regarded only as a partial component of the global membrane rigidness. Namely, the total dilatational surface modulus includes compression and shear components, $\varepsilon = K + G \approx E_{coh}/A \approx (\Delta E_{\parallel} + \Delta E_{\perp} + E_{int})/A$ (López-Montero et al., 2013). For the biologically relevant monolayers at high temperatures ($\pi_b \approx 30\, mN/m$; $T \approx 38\,\mathrm{oC}$), by taking structural data ($A \approx 0.9\, nm^2$ and $\Delta E_{\parallel} \approx 20 k_B T$; see Table 2) and assuming the Poisson ratio estimated earlier for the shear measurements ($\nu \approx 0.2$), we predict $K_b \approx (1 - 2\nu)\varepsilon \approx 70\, mN/m$, in qualitative agreement with our experiments (see Figure 6B). To summarize the impact of escin at mechanical equivalence with a highly rigid material, for solid-like escin-rich membranes interacting with lipids, we found constitutive properties recapitulated in the surface dilatational rigidity $\varepsilon_S = K + G$ (for $K \approx K_b$, $G \approx G_0' \gg K_b$, and $\nu \approx 0.2$). However, for fluid-like DMPC-rich monolayers, we found a similar finite compressibility ($K \approx K_b$) but a negligible shear stiffness ($G_0' \approx 0$, $\nu \approx 1$), giving rise to a lower dilatational rigidness (i.e., $\varepsilon_F = K \ll \varepsilon_S$). In the opposite case of solid-like monolayers of pure escin, we found the maximal values of the shear rigidity $G_{max}' \approx 200\, mN/m$ (Figure 5B) and the compression modulus $K_{max} \approx 200\, mN/m$ (Figure 6B), hence the dilatational modulus $\varepsilon_{esc} \approx 0.4\, N/m$ and the Poisson ratio $\nu_{esc} = (G - K)/(G + K) \approx 0$ (López-Montero et al., 2013), resulting in a global cohesive energy $E_{coh} = \varepsilon A \approx 90\, k_B T$. Such a parametric constitutive dataset ranks the surfactant β-escin top in the scale of fluid surface cohesivity and endows the record of surface rigidness for the uniform (monophasic) adsorption monolayers of a soluble compound (Kharbedia et al., 2021).

3.7.2 Interdomain interaction: mesoscopic fluidity

Nevertheless, we must remember that the hybrid DMPC–escin system can eventually remain in a heterogeneous biphasic state with solid escin-rich domains rafting the continuous DMPC-rich phase (see Figure 3). They can eventually lead to additional rigidities with dominant shear rigidity for the highest escin insertions. Hence, an intermediate mechanical impact is observed in these 2Φ-statuses, especially at low temperatures (see Figure 5; central panels). Hence, we visualize the global rigidness as a mesoscopic equivalent $\varepsilon_{eq} = \varepsilon_{eq} (\varepsilon_S, \varepsilon_F, \varepsilon_{dom})$, including the crowding interaction between the solid-like domains (ε_D) (Espinosa et al., 2011). Because a heterogeneous monolayer (raft-like) actually couples the phases' rigidities in parallel, we predict $\varepsilon_{eq}^{-1} = \phi \varepsilon_S^{-1} + (1 - \phi)\varepsilon_F^{-1} + \varepsilon_{dom}^{-1}$, where ϕ is the domain fraction) (Arriaga et al., 2010b). As far as the solid-like escin-rich domains interact with a remanent 2Φ-rigidness in ordered states, we thus expect $\varepsilon_{eq}^{(O)} \approx \varepsilon_D [1 - \frac{\varepsilon_{dom}}{K_b} (1 - \phi)]$, for instance, at high domain fractions (as experimentally observed at low temperatures $\phi \rightarrow 1$; see Figure 3). This formula shows the influence of the lateral interactions between domains on the effective rigidness of an ordered mosaic membrane (i.e., $\varepsilon_{eq}^{(O)} \approx \varepsilon_D$ at $\phi \rightarrow 1$). However, for the fluid liquid-disordered phase $\varepsilon_{eq}^{(D)} \approx K_b \ll \varepsilon_{eq}^{(O)}$. By investigating the experimental data in Figures 5, 6 in the highly ordered state at low temperatures, we estimated this quantity as the interdomain interaction energy $\varepsilon_{eq}^{(O)} \approx G_{2\Phi}' + K_b \approx 70 mN/m \approx 17 k_B T/nm^2 \approx \varepsilon_D$ (as calculated per molecule). However, in the highly disordered state at high temperature, we estimated $\varepsilon_{eq}^{(D)} \approx K_b \approx 50 mN/m \approx 20 k_B T/nm^2$, corresponding to the laterally homogeneous interaction between DMPC and escin at the physiological bilayer state (i.e., $\Delta E_{\parallel} \approx K_b$). These mechanical estimations are in qualitative agreement with our previous experimental calculations from the kinetic measurements (see Tables 1, 2; Section 3.5) and more sophisticated theoretical estimates inferred for heterogeneous membranes (Arriaga et al., 2008; Catapano et al., 2011; Espinosa et al., 2011; Langevin and Monroy, 2014). However, being elastically Hookean corresponding to the relatively low interaction energies put into play at the small deformations considered, all the monolayers studied in this linear, weakly dissipative regime undergo Newtonian viscous flow at correspondingly low deformation rates (see Figure 5: right panels).

3.8 Nonlinear regime: soft solid behavior

The rheological data showed a nonlinear softening behavior, clearly evidenced for the pure escin monolayers as a plastic plateau above yield stress (see Figure 5A). They exhibited an evident dissipative origin: first, a decrease in the apparent shear modulus as the consequence of the stress softening above the yield point (the elastic stress $\sigma_{elas} = G' \gamma$ with $G' < G_0'$ for $\gamma > \gamma_Y^{(esc)} \approx 1\,\%$; Figure 5B) and second, shear thinning shown by the shear viscosity of pure escin monolayers with values significantly lower than the shear stiffness in both temperature regimes ($G'/\omega \gg G''/\omega = \eta_0 \geq 0.01\, N\, s/m$; Figure 5C). In the Newtonian regime, the dynamic viscosity appeared as the linear response to frictional losses at low shear rates below the yield point [i.e., the frictional stress (the frictional stress $\sigma_{fric} = \eta_0 \dot{\gamma}$ with $\eta_0 \equiv G''/\omega \ll \sigma_{elas}/\omega\gamma$ for $\gamma < \gamma_Y^{(esc)} \approx 1\,\%$ and $\dot{\gamma} < \dot{\gamma}_Y^{(esc)} \approx 0.1\ \mathrm{s}^{-1}$; Figure 5C]. Arguably, the surface friction primarily arises from the dissipation of the cohesion energy that retains the surface molecules adsorbed for longer than the diffusion time, that is, $E_{ads} \Rightarrow \Delta E_{\perp} \approx G''A$ (Evans and Hochmuth, 1976; Espinosa et al., 2011; Hermans and Vermant, 2014) by taking the kinetic data measured for pure escin monolayers in the high compaction low-temperature status and $E_{ads} \Rightarrow -\Delta E_{\perp} \approx 12 k_B T$ and $\tau_D \approx 10^2\, s$, by taking $\delta A_{esc} \approx 0.3\, nm^2$ [see Figure 3 and Table 2 in Section 3.4; for $A \Rightarrow A_{esc} \approx 0.9\, nm^2$ (Dargel et al., 2019; Geisler et al., 2020a)]. Assuming a diffusional strain rate well within the Newtonian regime $\dot{\gamma}_D = \tau_D^{-1} (\delta A_{esc}/A_{esc}) \approx 0.003\, s^{-1}$ $(\ll \dot{\gamma}_Y^{(esc)} \approx 0.1\ \mathrm{s}^{-1})$, we estimate in this regime the highest frictional losses as $\omega\eta_0 \approx G'' \geq \Delta E_{\perp}/A_{esc} \approx 10 mN/m$, corresponding to the shear viscosity $\eta_0 \approx G''/\omega \geq 0.01\, N\, s/m$ (in agreement with the experimental data at $\omega = 1\, Hz$). Above the diffusional yield point ($\dot{\gamma}_D$), shear thinning follows the characteristic of a soft viscoelastic solid ($\eta \ll \eta_0$ for $\gamma \gg \dot{\gamma}_Y^{(esc)} \approx 0.1\ \mathrm{s}^{-1}$) (see Figure 5; right panels). The stress-softened monolayers display apparent values of the shear modulus comparatively higher than those of the loss modulus (i.e., $G_0' \gtrsim G_0'' = \omega\eta_0$ for soft solids), hence defining the viscoelastic status of the monophasic (pure) escin monolayer to be predominantly a soft solid under weakly perturbed mechanical equilibrium. This very particular rheological behavior assigns the bare escin monolayers with the mechanical characteristics typical of a two-dimensionally viscoelastic material able to support high shear stress—a soft solid exhibiting one of the highest values of shear rigidity reported to date for surface films supported on liquid surfaces (Kharbedia et al., 2021). For the bare DMPC monolayers, however, the liquid crystalline lipid arrangement undergoes linear deformation over the entire range of strains (Figure 5; left panels), hence becoming able to deform fluid-like (i.e., $G' = 0$; central panels). As expected, the shear viscosities of the DMPC monolayers are significantly smaller than those of the escin monolayers (left panels). Therefore, the liquid crystalline mesophases of the bare DMPC monolayers are considered to behave essentially fluid-like in mechanical terms, similar to viscous fluid, not only in the high-temperature L$_\mathrm{D}$-phase but also in the low-temperature L$_\mathrm{O}$-phase [i.e., $G'' = \omega\eta \gg G' = 0$ for fluids (Espinosa et al., 2011)].

For the binary monolayers of liquid-like escin–DMPC, since transversely penetrated by solid-like escin, the biphasic monolayer was observed to produce an intermediate rheological scenario (see Figure 3). At low temperatures, we detected a dominance of the solid escin domains in the linear part of the stress–strain plot (in both temperature regimes, we detected $G_0' \geq G_0'' = \omega\eta_0$; see Figure 5B). Owing to the mesoscopic ordering induced by the solid escin-rich domains into the continuous Lo-phase of DMPC at low temperatures (as recording nonlinear shear responses at $T = 4oC$), we detected $G_0' \gg G_0'' \gg 0$ in the widely explored range of deformations. We also detected a plastic yield now appearing shifted up to shear deformations higher than those observed for pure escin ($\gamma_Y^{(mix)} \approx 5\,\% > \gamma_Y^{(esc)} \approx 1\%$). Such a low-temperature DMPC-rich phase seemed extrinsically rigidified by integrating escin from the subphase (similar to a confined liquid crystal). However, it could not retain shear stress above the yield point (similar to a high-viscosity liquid crystal under plastic flow). Differently, the high-temperature (liquid-like) mesophases of the binary DMPC–escin system behaved rheologically similar to the bare DMPC monolayer (with recording shear responses at 38°C, we detected $G_0'' \gg G_0' = 0$; see Figure 5C). As far as the disordered DMPC L$_\mathrm{O}$-phase could be intrinsically penetrated by escin at high temperatures (above $T_m \approx 23\, oC$), the solid character of the escin-rich domains of the biphasic DMPC–escin systems persisted dominant only at low temperatures (at $T \ll T_m$) and low deformation strain ($\gamma \ll \gamma_Y^{(mix)}$). In contrast, the phase-separated DMPC–escin monolayer behaved essentially fluid-like at high temperatures ($T \gg T_m$) and high deformations ($\gamma \gg \gamma_Y^{(mix)}$), similar to a fragile glassy material. In summary, although the rigidity modulus was practically null (or undetectable) in DMPC-rich monolayers, as expected for liquid-like phospholipid membranes above the melting transition, the adsorption association with underlying solid escin imparted enough shear rigidity to make the hybrid DMPC–escin membranes behave similar to a soft solid material.

3.9 Surface dynamics in the frequency domain: soft glassy rheology

In rheological terms, a typical soft solid is dynamically characterized by a weak dependence of the viscoelastic moduli on the deformation frequency. Particularly, in the Hookean (linear) regime, the rigidity modulus and the slightly lower loss modulus are expected to scale with a similar power law as $G' \sim G'' \sim \omega^x$ (with $x \ll 1$), a behavior widely known as soft glassy rheology, or briefly SGR (Sollich et al., 1997; Srivastava et al., 2011). To further evaluate the dynamic behavior of escin-containing membranes (in Langmuir monolayers spread at the A–W interface), we analyzed the frequency dependence of the viscoelastic moduli in the structural scenarios described earlier. Figure 7 shows the experimental results by comparing the rheological behavior of the binary escin–DMPC monolayers with the single component systems. In the case of pure escin monolayers, the viscoelastic moduli were found with similar absolute values in high-T and low-T states and frequency dependencies compatible with SGR behavior (Figure 7A).

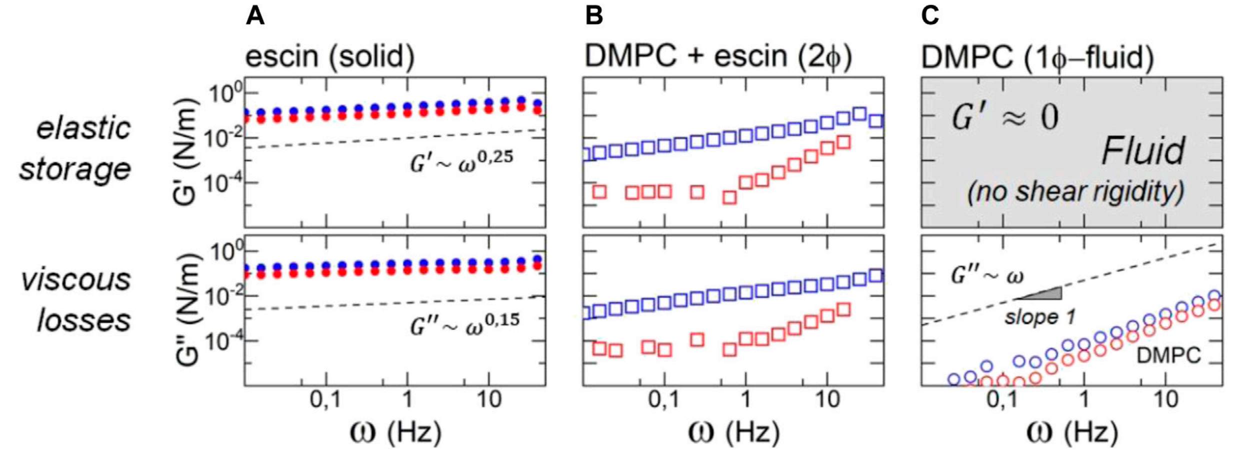

FIGURE 7
Frequency dependence of the surface shear rheology of escin–DMPC monolayers in the linear regime of shear deformation for the biological regulation status at $\pi_b = 30mN/m$ (elastic storage: upper panels; viscous losses; lower panels). Measurements performed in triplicate; standard deviation 10% typical (compatible with the dot size). We show comparative graphs of pure escin [monophasic 1ϕ; **(A)**], escin interacting with DMPC penetrating from the aqueous subphase at concentration of 0.1 mM [biphasic 2ϕ **(B)**], and pure DMPC [1ϕ **(C)**] at 4°C (blue symbols), and 38°C (red symbols).

Remarkably, we obtained extremal values of shear rigidity (ca. 100 mN/m), even higher than those of the extremely rigid ceramide molecule (López-Montero et al., 2010; Catapano et al., 2011; Castro et al., 2014), an essential messenger involved in cell apoptosis (Catapano et al., 2017; Alonso and Goñi, 2018).

On the one hand, we detected the solid-like escin monolayers behaving SGR-like with a shear modulus displaying a weak 5power-law dependency ($G' \approx G_0^{'}\omega^{0.25}$ under amplitude $G_0^{'} = 120 \pm 10mN/m$), found even weaker for the loss modulus ($G'' \approx G_0^{''}\omega^{0.15}$ under amplitude $G_0^{''} = 110 \pm 10mN/m$). On the other hand, we detected the liquid-like DMPC monolayers behaving in a purely Newtonian fluid scenario at vanishing rigidness at low and high temperatures (i.e., $G' \approx 0$ and $G'' \approx \omega\eta_0$), corresponding to a time-independent value of the dynamic viscosity (η_0). For DMPC, we measured shear viscosity decreasing with increasing temperature, corresponding to Newtonian fluids (see Figure 7C; bottom). For the binary DMPC–escin monolayers, however, a completely different behavior was observed (Figure 7B). When escin is inserted into the biphasic DMPC monolayer at a low temperature (2Φ), a high shear rigidness remains ($G_0^{'} = 100 \pm 20mN/m$), although displaying a stronger frequency dependency ($G' \approx G_0^{'}\omega^{0.5}$), significantly higher than expected for canonical SGR behavior in a rigid solid ($x \approx 0$). A similar behavior was found at low temperatures for the loss modulus ($G'' \approx G_0^{''}\omega^{0.5}$ with amplitude $G_0^{''} = 90 \pm 20mN/m$). Because $G_0^{'} \approx 100mN/m \gtrsim G_0^{''}$ in this solid-like phase-separated state (2Φ, low-T), we assigned it with SGR-like behavior typical for a soft solid. At high temperatures for the monophasic liquid-like phase (1Φ, high-T), the elastic and loss moduli had finite absolute values albeit relatively inverted, corresponding to a predominantly fluid viscoelastic material ($G_0^{''} \approx 90mN/m \gtrsim G_0^{'}$). A completely different dynamics was observed breaking out the solid-like SGR behavior typical for shear deformations at low frequencies ($\omega < \omega_c \approx 1\,Hz$) up to liquid-like behavior observed at higher frequencies ($\omega > \omega_c$; see Figure 6; central panels). Such dynamic bimodality occurred through a characteristic diffusive crossover ($\omega_c \approx \tau_D^{-1} \approx 1\,Hz$), compatible with the observed dual diffusion–reorganization kinetics (see Figure 4). At lower frequencies ($\omega \ll \omega_c$), the slowly deformed DMPC–escin monolayer behaved like a soft glassy solid as far as the much faster diffusive exchanges with the bulk were blocked. At higher frequencies ($\omega \gg \omega_c$), however, the monolayer deformed quickly and behaved like a regular fluid. It is a viscoelastic material that can relax stresses through dynamically congruent adsorption–desorption exchanges with the bulk. Therefore, the rheological dynamic bimodality revealed for the binary DMPC–escin monolayers could be plausibly connected with the dual phase behavior discussed earlier in structural terms. Because these molecules could partially segregate into two phases of model systems at the dependence of temperature, one with a higher phospholipid content behaving liquid-like and the other with a higher escin content behaving solid-like, such mechanical duality enabled the emergence of complex rheology with a probable biological impact owing to rigidness in mosaic membranes such as receiving natural saponins, for example, from functional feeding, or dietary supplements for some therapies.

4 Discussion

This study addressed the physicochemical role of β-escin in the functional regulation of mosaic membrane mechanics recreated in model systems. In biomedical terms, this natural saponin acts as a phlebotonic medicine used, for instance, to treat chronic CVI. We showed the amphiphilic character of escin, conferring a dual mechanical impact on model membranes. Membrane escin is prone to either self-aggregate extrinsically into rigid solid phases that cause local stiffening but fluidization under mesoscopic disorder or intrinsic compaction with other membrane components that also produce rigidification but a global decrease in fluidity. The experiments performed here with model systems demonstrate membrane escin incorporation either intrinsically along the longitudinal in-plane integration mode or extrinsically across the transverse out-of-plane penetration. These insertion pathways differently impact the effective rheology of the escin-modified membrane. If escin is internally incorporated into the lipid membrane (intrinsic longitudinal integration), the system immediately raises the mechanical equilibrium as a soft, glassy solid more rigid than fluid. However, when escin is externally incorporated from the adjacent subphase (extrinsic transverse insertion), a bimodal adsorption mechanism emerges, governed by bulk diffusion–membrane reorganization, leading to more fluid than rigid behavior. In particular, when adsorbed from the bulk on a phospholipid membrane surface, a thin saponin layer adsorbs the surface from its outer side to become later integrated as a hybrid escin–lipid membrane. First, the transversely incorporated molecules extrinsically promote phase segregation, leading to structural disorganization (during the initial steps of adhesive membrane adsorption). Later, intrinsic molecular condensation leads to local structuration followed by equilibrium (during terminal cohesive relaxation). These dual dynamic behaviors emerge from the multiple scales involved in the adsorption–insertion process, as described by the BPGP theory (Buttler, 1932; Pethica, 1955; Graham and Phillips, 1979; Fainerman and Vollhardt, 1999) from the bottom scale of the diffusing escin monomers dissolved in the bulk subphase, through the intermediate bulk–surface infrastructure (where they adhere and reorganize within the polar heads of the membrane components) up to the superior membrane superstructure (where cohesive escin and adhesive membrane interact, constituting a heterogeneous quasi-2D system able to undergo mesoscale phase transitions) (refer to Dukhin et al., (1994), for a comprehensive monography on adsorption dynamics at fluid interfaces. Although such a class of condensing interactions, here mediated by solid-like escin, is also frequent in other adhesive systems, such as single sugars (Koster et al., 1994) and small nanoparticles (Salassi et al., 2021; Kariuki et al., 2022), the amphiphilic quadrupole in escin imposes a very particular surface bidirectional cohesivity that makes membrane interactions dual in raising enhanced stability, which can extrinsically adhere more bulk material and intrinsically compact the already inserted material.

As a relevant contribution to membrane mechanics, our complementary measurements of compression modulus (K) and shear rigidity (G) demonstrated the key role of the dilatational rigidness ($\varepsilon = K + G$) as the global descriptor of molecular compaction necessary for functional membrane stability. Although the ordering rigidness at low temperatures was evidenced to govern the escin–phospholipid membranes into solid-like heterogeneous arrangements of membrane rafts (more rigid than fluid), mechanical softening concomitant with viscoelastic behavior was observed to dominate the homogeneous fluid membranes at high temperatures (more fluid than rigid). The surface shear rigidity and compression modulus were revealed to be controlled by the lateral compaction energy ($-\Delta E_{\parallel} \approx 20 - 12 k_B T$ per molecule), whereas the shear viscosity increased with the strength of the transverse attractive potential between the supporting surface and underlying escin ($-\Delta E_{\perp} \approx 12\, k_B T$ per molecule). In the case of escin-rich membranes, the high longitudinal attraction between the aglycones made the corresponding frictional losses very high and dependent on the higher shear rates. Above the diffusional frequency, shear-thinning (fluidization) appeared, in which the viscosity decreased due to the transverse ejection of escin. As expected for pure DMPC, the membrane viscosity was independent of the shear rate. This Newtonian behavior was characteristic of the high fluidity of unsaturated phospholipids compared to the high stiffness of pure escin. For the mixed DMPC–escin case resembling a composite biomembrane at low temperatures, the monolayer exhibited a pseudoplastic solid-like behavior compatible with soft glassy rheology. However, at high temperatures, a Newtonian fluid-like behavior emerged; herein, the system flowed like the natural phospholipid membrane. After the membrane stiffening transition owned by the cohesive properties of the saponin-lipid assembly, escin began to nucleate as an aggregated phase of aglycone moieties interacting by hydrophobicity within the lipid bilayer. This nucleation was favored by the pre-existing ordering of the lipids; the greater the order, the greater the capacity for DMPC-scaffolded insertion and further reorganization of the saponin in the lipid assembly, which promoted higher rigidness under regulated frictional losses.

Our experimental results support the hypothesis of the compacting incorporation of escin, depending not only on the solid or fluid DMPC-phase state, but also on the vectorized direction particularly chosen for escin insertion (longitudinal along membrane traffic or transverse across bulk diffusion). We demonstrated that the pre-existing molecular ordering acted as a mechanical scaffold with a dual mechanical function, a key regulator of membrane rheology. Escin elicited either structural stiffening or dynamic softening, depending on the molecular orientation adopted during the incorporation process (longitudinal or transverse, respectively). When the escin molecules became an integral part of the membrane assembly (which would represent a longitudinal insertion similar to natural bilayer assembly $E_{int} > \Delta E_{\parallel} \gg \Delta E_{\perp}$), they tended to associate with the phospholipids to laterally segregate into two heterogeneous phases. This phase segregation is similar to the cholesterol-driven formation of rafts in eukaryotic biomembranes (Simons and Ikonen, 1997). The interaction energies that dominated the raft assembly over the relevant micro- and meso-scales resulted from the strong surface adhesivity of escin, not only in the form of molecular cohesion between aglycone moieties but also as mesoscopic cohesivity between domains (Arriaga et al., 2010b). This stabilizing mosaic rigidness appeared as a multiscale class of membrane ordering scaffolded by the parental lipid order. Hence, emergent properties were shown against disruptive dilatation as encoded by the cohesive energy, $E_{coh} = \varepsilon A \Rightarrow (K + G)A$ (Singer and Nicolson, 1972; Simons and Ikonen, 1997; Sprong et al., 2001; Van Meer et al., 2008; Philips et al., 2009). For β-escin, we estimated $E_{coh}\,(= E_{int} + \Delta E_{\parallel} + \Delta E_{\perp}) = \varepsilon A \approx 90\, k_B T$. This high cohesivity per molecule was ranked top in soluble surfactants, even higher than those of rigid insoluble lipids, such as ceramide (López-Montero et al., 2010). The highest surface rigidity supported hydrodynamic crystallization in water surfaces (Kharbedia et al., 2021).

4.1 Membrane escin incorporation causing stiffening and fluidization

For physicochemical analysis of the escin–membrane interaction, the amphiphilic molecule escin was presented at a constant submicellar concentration such that membrane insertion occurred from the monomer status (at $c = 10^{-4}\,M < CMC$) (Böttcher and Drusch, 2017; Sreij et al., 2017; Geisler et al., 2020a; Kharbedia et al., 2021). Under submicellar escin incorporation, the intrinsic membrane ordering increased at longer adsorption times to strongly hinder the transverse diffusivity, making the membrane the most packed. Although the lateral freedom within the escin-rich membrane domains was highly crowded, mosaic phase segregation promoted the membrane to fluidify. Hence, mesoscopic fluidity emerged when the continuous phase appeared more fluid (composed of molten phospholipids) than the discrete, more rigid domains (enriched in escin). Subsequently, a mechanical tradeoff was shown between the cohesive escin–lipid interactions (enthalpic) and the disordering domain interactions (entropic). The composite mosaic structure imparted effective fluidity through the continuous incompressible phase of liquid crystalline lipids (Arriaga et al., 2008; Arriaga et al., 2010b; Langevin and Monroy, 2014). Such rheological diaphony led to mesoscopic fluidity within heterogeneous escin–DMPC membranes, implying synergistically dual functional mechanics rather than negative antagonism.

Mechanical duality is not rare in complex models of membrane heterogeneity, endowing the compositional mosaicity typical of biological membranes (Finegold, 1992). Likewise, a plausible functional paradigm for mosaic membranes could emerge from the dual membrane energetics observed here for solid-like escin exchanging with the fluid-like lipid membrane. This cohesive energetics was revealed as heterogeneous as locally governed by the condensation status of the exchanging molecules, either extrinsic or intrinsic. Local membrane condensation (cf. mosaicity) determined the adsorption–reorganization kinetics, leading to cohesive diffusivities.

4.2 Membrane escin as a therapeutic agent

The mechanical duality that emerged from the saponin–phospholipid assembly could play an important role in the therapeutic efficacy of pharmacological procedures involving aglycone moieties interacting with membrane phospholipids. In particular, the β-escin could promote dual cell rigidness, softening, or both at interference with membrane sterols and other structural mediators of membrane rigidness and fluidity (Güçlü-Üstündağ and Mazza, 2007; Sreij et al., 2019; Geisler et al., 2020b; Glickman et al., 2020). The medicinal extract from chestnut seeds (*A. hippocastanum*), standardized for the content of β-escin, is currently used as an efficient and toxicologically safe oral treatment for CVI (Underland et al., 2012). For years, escin has been proven to be highly bioavailable, non-toxic, safe, and well-tolerated under oral ingestion (Liehn et al., 1972; Loew et al., 2000). No new safety concerns were identified in the updated Cochrane review, published in 2012 (Underland et al., 2012). The usual therapeutic dose is 100 mg of escin per day (Underland et al., 2012), although higher doses, up to 100 times, are admitted as dietary supplements (Pittler and Ernst, 2012). In an adult human, the admitted dosages are on the safety interval $1^{-}100\text{mg}/kg - day$ roughly corresponding to concentrations ranging $10^{-6} - 10^{-4\text{M}}$ (total biodistribution). Our physicochemical conclusions were obtained in the upper limit of the biomedical operativity interval (ca. 10^{-4} M), which means adequate and sufficient escin–membrane interaction to raise etiology-relevant conclusions. Clinical trials on phlebotonic efficiency *in vivo* demonstrated that oral ingestion of chestnut seed extract containing 50 mg escin resulted in a maximal plasma concentration within the therapeutic interval $c_{max}^{(ther)} \approx 6 - 20\,ng/mL \approx 10^{-8\text{M}}$ (Loew et al., 2000; Pittler and Ernst, 2012). However, considerable variability between the different clinical studies was clarified (Liehn et al., 1972; Loew et al., 2000; Pittler and Ernst, 2012). With respect to phlebotonic efficiency assessed *in vitro*, a dose-response study performed using human saphenous vein preparations indicated a 10%–20% increase in venous tone, already clinically meaningful, well evident at dosing concentrations even below 10^{-7} M (Sirtori, 2001). Therefore, submicellar concentrations, even extremely low, as considered in the physicochemical terms of mechanical membrane impact, seem to be therapeutically efficient in the biomedical setting (i.e., $c_{max}^{(ther)} \approx 10^{-8\text{M}} \ll c^{(mech) < CMC}$).

By varying the dose of the membrane-active saponin, its therapeutic efficacy could be subsequently modulated under mechanical changes induced by its vectorized incorporation into the cell membrane (either transverse by extrinsic diffusivity or longitudinal by intrinsic lipid traffic). Therefore, the present results represent a relevant physicochemical insight, opening new avenues for membrane-targeted pharmacological treatments of venous inflammation based on saponins. Mechanically behaving as solids and liquids, these pharmacologically active molecules (phlebotonics), particularly β-escin, could dually render into structural rigidness and fluidity with a therapeutic value in the cellular membranes of the pathogenic venous vasculature.

Data availability statement

The original contributions presented in the study are included in the article/supplementary material. Further inquiries can be directed to the corresponding authors.

Author contributions

LM, DH-A, MM-R, NC, CD, and RG conducted research, provided experimental data, and contributed to data. JS, TH, and FM supervised the research and drafted the manuscript. TH and FM supported the search for funding, planned and supervised the research, contributed to data analysis, and wrote the manuscript. All authors contributed to the article and approved the submitted version.

Funding

LM was contracted by the María Zambrano Program from Ministerio de Universidades de España for the attraction of international talent under Next-Generation European Union funding (Grant CT19/22). This work was supported by the Spanish Ministry of Science and Innovation (MICINN–Agencia Española de Investigación AEI) under Grants PID 2019-108391RB-100 and TED2021-132296B-C52 (to FM) and Comunidad de Madrid under Grants S2018/NMT-4389 and Y2018/BIO-5207 (to FM). The authors also acknowledge the financial support of the German Research Foundation DFG Grant HE 2995/7-1 (to TH) and the Open Access Publication Fund of Bielefeld University for the publication costs. This study was also funded by the REACT-EU program PR38-21-28 ANTICIPA-CM, a grant by Comunidad de Madrid and the European Union under the FEDER program in response to the COVID-19 pandemic.

Acknowledgments

The authors acknowledge Prof. Juan J. Giner-Casares for making available Langmuir troughs and the BAM facility in his laboratory at Universidad de Cordoba and also for fruitful discussions on the monolayer domain morphologies. LM gratefully thanks him for hospitality.

Conflict of interest

Publisher's note

References

Al-Rekabia, Z., and Contera, S. (2018). Multifrequency AFM reveals lipid membrane mechanical properties and the effect of cholesterol in modulating viscoelasticity. *Proc. Nat. Acad. Sci.* 115, 2658–2663. doi:10.1073/pnas.1719065115

Alonso, A., and Goñi, F. M. (2018). The physical properties of ceramides in membranes. *Annu. Rev. Biophys.* 47, 633–654. doi:10.1146/annurev-biophys-070317-033309

Arriaga, L. R., López-Montero, I., Ignés-Mullol, J., and Monroy, F. (2010b). Domain-growth kinetic origin of nonhorizontal phase coexistence plateaux in Langmuir monolayers: compression rigidity of a raft-like lipid distribution. *J. Phys. Chem. B* 114, 4509–4520. doi:10.1021/jp9118953

Arriaga, L. R., López-Montero, I., Orts-Gil, G., Farago, B., Hellweg, T., and Monroy, F. (2009). Fluctuation dynamics of spherical vesicles: frustration of regular bulk dissipation into subdiffusive relaxation. *Phys. Rev. E.* 80, 031908. doi:10.1103/PhysRevE.80.031908

Arriaga, L. R., López-Montero, I., Rodríguez-García, R., and Monroy, F. (2008). Nonlinear dilational mechanics of Langmuir lipid monolayers: A lateral diffusion mechanism. *Phys. Rev. E* 77, 061918. doi:10.1103/PhysRevE.77.061918

Arriaga, L. R., Rodriguez-Garcia, R., López-Montero, I., Farago, B., Hellweg, T., and Monroy, F. (2010a). Dissipative curvature fluctuations in bilayer vesicles: coexistence of pure-bending and hybrid curvature-compression modes. *Eur. Phys. J. E* 31, 105–113. doi:10.1140/epje/i2010-10551-1

Azzam, R. M. A., and Bashara, N. M. (1992). *Ellipsometry polarized light*. 1. North-Holland: Bruker.

Baumgart, T., Hunt, G., Farkas, E. R., Webb, W. W., and Feigenson, G. W. (2007). Fluorescence probe partitioning between Lo/Ld phases in lipid membranes. *Biochim. Biophys. Acta* 68, 2182–2194. doi:10.1016/j.bbamem.2007.05.012

Böttcher, S., Keppler, J. K., and Drusch, S. (2017). Mixtures of Quillaja saponin and beta-lactoglobulin at the oil/water-interface: adsorption, interfacial rheology and emulsion properties. *Colloids Surf. A* 518, 46–56. doi:10.1016/j.colsurfa.2016.12.041

Böttcher, S., and Drusch, S. (2017). Saponins — self-assembly and behavior at aqueous interfaces. *Adv. Colloid Interf. Sci.* 243, 105–113. doi:10.1016/j.cis.2017.02.008

Brunauer, S., Emmett, P. H., and Teller, E. (1938). Adsorption of gases in multimolecular layers. *J. Am. Chem. Soc.* 60, 309–319. doi:10.1021/ja01269a023

Buttler, J. A. V. (1932). The thermodynamics of the surfaces of the solutions. *Proc. R. Soc. A* 138, 348. doi:10.1098/rspa.1932.0040

Castro, B. M., Prieto, M., and Silva, L. C. (2014). Ceramide: A simple sphingolipid with unique biophysical properties. *Prog. Lipid Res.* 54, 53–67. doi:10.1016/j.plipres.2014.01.004

Catapano, E. R., Arriaga, L. R., Espinosa, G., Monroy, F., Langevin, D., and López-Montero, I. (2011). Solid character of membrane ceramides: A surface rheology study of their mixtures with sphingomyelin. *Biophys. J.* 101, 2721–2730. doi:10.1016/j.bpj.2011.10.049

Catapano, E. R., Natale, P., Monroy, F., and López-Montero, I. (2017). The enzymatic sphingomyelin to ceramide conversion increases the shear membrane viscosity at the air-water interface. *Adv. Colloid. Interf. Sci.* 247, 555–560. doi:10.1016/j.cis.2017.07.014

Cheok, C. Y., Salman, H. A. K., and Sulaiman, R. (2014). Extraction and quantification of saponins: A review. *Food Res. Int.* 59, 16–40. doi:10.1016/j.foodres.2014.01.057

Cogolludo, A., Villamor, E., Perez-Vizcaino, F., and Moreno, L. (2019). Ceramide and regulation of vascular tone. *Int. J. Mol. Sci.* 20, 411. doi:10.3390/ijms20020411

Dargel, C., Geisler, R., Hannappel, Y., Kemker, I., Sewald, N., and Hellweg, T. (2019). Self-assembly of the biosurfactant aescin in solution: A small-angle X-ray scattering and fluorescence study. *Colloids Interf.* 3, 47. doi:10.3390/colloids3020047

De Groot, C., Müsken, M., and Müller-Goymann, C. C. (2018). Novel colloidal microstructures of β-escin and the liposomal components cholesterol and DPPC. *Planta Medica* 84, 1219–1227. doi:10.1055/a-0624-2706

Deseri, L. (2017). "Elasticity and hereditariness," in *The role of mechanics in the study of lipid bilayers. CISM international centre for mechanical sciences.* Editor E. J. Steigmann (Cham: Springer). doi:10.1007/978-3-319-56348-0_2

Díez-Pascual, A. M., Monroy, F., Ortega, F., Rubio, R. G., Miller, R., and Noskov, B. A. (2007). Adsorption of water-soluble polymers with surfactant character. Dilational viscoelasticity. *Dilational Viscoelasticity Langmuir* 23, 3802–3808. doi:10.1021/la062936c

Dudek-Makuch, M., and Studzińska-Sroka, E. (2015). Horse chestnut – efficacy and safety in chronic venous insufficiency: an overview. *Rev. Bras. Farmacogn.* 25, 533–541. doi:10.1016/j.bjp.2015.05.009

Dukhin, S. S., Kretzschmar, G., and Miller, R. (1994). *Dynamics of adsorption at liquid interfaces: Theory, experiment, application*. Amsterdam, Netherlands: Elsevier.

Elekofehinti, O. O., Iwaloye, O., Olawale, F., and Ariyo, E. O. (2021). Saponins in cancer treatment: current progress and future prospects. *Pathophysiology* 28, 250–272. doi:10.3390/pathophysiology28020017

Espinosa, G., López-Montero, I., Monroy, F., and Langevin, D. (2011). Shear rheology of lipid monolayers and insights on membrane fluidity. *Proc. Nat. Acad. Sci.* 108, 6008–6013. doi:10.1073/pnas.1018572108

Evans, E. A., and Hochmuth, R. M. (1976). Membrane viscoelasticity. *Biophysical J.* 16, 1–11. doi:10.1016/S0006-3495(76)85658-5

Fainerman, V. B., and Vollhardt, D. (1999). Equations of state for Langmuir monolayers with two-dimensional phase transitions. *J. Phys. Chem. B* 103, 145–150. doi:10.1021/jp983109q

Finegold, L. X. (1992). *Cholesterol in membrane models*. 1. Florida: CRC Press.

Gallelli, L. (2019). A review of its anti-edematous, anti-inflammatory, and venotonic properties. *Drug Des. devel. Ther.* 13, 3425–3437. doi:10.2147/DDDT.S207720

Gauthier, C., Legault, J., Girard-Lalancette, K., Mshvildadze, V., and Pichette, A. (2009). Haemolytic activity, cytotoxicity and membrane cell permeabilization of semi-synthetic and natural lupane- and oleanane-type saponins. *Bioorg. Med. Chem.* 17, 2002–2008. doi:10.1016/j.bmc.2009.01.022

Geisler, R., Dargel, C., and Hellweg, T. (2020a). The biosurfactant β-aescin: A review on the physico-chemical properties and its interaction with lipid model membranes and Langmuir monolayers. *Molecules* 25, 117. doi:10.3390/molecules25010117

Geisler, R., Pedersen, M. C., Hannappel, Y., Schweins, R., Prévost, S., Dattani, R., et al. (2019). Aescin-induced conversion of gel-phase lipid membranes into bicelle-like lipid nanoparticles. *Langmuir* 35, 16244–16255. doi:10.1021/acs.langmuir.9b02077

Geisler, R., Prévost, S., Dattani, R., and Hellweg, T. (2020b). Effect of cholesterol and ibuprofen on DMPC-β-aescin bicelles: A temperature-dependent wide-angle X-ray scattering study. *Crystals* 10, 401. doi:10.3390/cryst10050401

Glickman, D., García Rey, N., Richert, M., Meister, K., and Braunschweig, B. (2020). pH effects on the molecular structure and charging state of β-Escin biosurfactants at the air-water interface. *J. Colloid Interface Sci.* 607, 1754–1761. doi:10.1016/j.jcis.2021.09.086

Golemanov, K., Tcholakova, S., Denkov, N., Pelan, E., and Stoyanov, S. D. (2013). Remarkably high surface viscoelasticity of adsorption layers of triterpenoid saponins. *Soft Matter* 9, 5738–5752. doi:10.1039/C3SM27950B

Golemanov, K., Tcholakova, S., Denkov, N., Pelan, E., and Stoyanov, S. D. (2014). The role of the hydrophobic phase in the unique rheological properties of saponin adsorption layers. *Soft Matter* 10, 7034–7044. doi:10.1039/C4SM00406J

Graham, D. E., and Phillips, C. (1979). Proteins at liquid interfaces. *J. Colloid Interface Sci.* 70, 403–414. doi:10.1016/0021-9797(79)90048-1

Güçlü-Ustündağ, O., and Mazza, G. (2007). Saponins: properties, applications and processing. *Crit. Rev. Food Sci. Nutr.* 47, 231–258. doi:10.1080/10408390600698197

Gwozdzinski, L., Bernasinska-Slomczewska, J., Hikisz, P., Wiktorowska-Owczarek, A., Kowalczyk, E., and Pieniazek, A. (2023). The effect of diosmin, escin, and bromelain on human endothelial cells derived from the umbilical vein and the varicose vein: A preliminary study. *Biomedicines* 11, 1702. doi:10.3390/biomedicines11061702

Helfrich, W. (1973). Elastic properties of lipid bilayers — theory and possible experiments. *Z. Naturforsch C* 28, 693–703. doi:10.1515/znc-1973-11-1209

Hermans, E., and Vermant, J. (2014). Interfacial shear rheology of DPPC under physiologically relevant conditions. *Soft Matter* 10, 175–186. doi:10.1039/C3SM52091A

Hill, R. M., and Dissado, L. A. (1985). Debye and non-Debye relaxation. *J. Phys. C. Solid State Phys.* 18, 3829–3836. doi:10.1088/0022-3719/18/19/021

Hormel, T. T., Kurihara, S. Q., Brennan, M. K., Wozniak, M. C., and Parthasarathy, R. (2014). Measuring lipid membrane viscosity using rotational and translational probe diffusion. *Phys. Rev. Lett.* 112, 188101. doi:10.1103/PhysRevLett.112.188101

Hostettmann, K., and Marston, A. (1995). *Saponins*. Cambridge: Cambridge University Press.

Jeon, J., and Voth, G. A. (2005). The dynamic stress responses to area change in planar lipid bilayer membranes. *Biophys. J.* 88, 1104–1119. doi:10.1529/biophysj.104.052183

Kariuki, R., Penman, R., Bryant, S. J., Orrell-Trigg, R., Meftahi, N., Crawford, R. J., et al. (2022). Behavior of citrate-capped ultrasmall gold nanoparticles on a supported lipid bilayer interface at atomic resolution. *ACS Nano* 16, 17179–17196. doi:10.1021/acsnano.2c07751

Kharbedia, M., Caselli, N., López-Menéndez, H., Enciso, E., Santiago, J. A., Herráez-Aguilar, D., et al. (2021). Moulding hydrodynamic 2D-crystals upon parametric Faraday waves in shear-functionalized water surfaces. *Nat. Commun.* 12, 1130. doi:10.1038/s41467-021-21403-0

Koczurkiewicz, P., Czyż, J., Podolak, I., Wójcik, K., Galanty, A., Janeczko, Z., et al. (2015). Multidirectional effects of triterpene saponins on cancer cells - mini-review of *in vitro* studies. *Acta Biochim. Pol.* 62, 383–393. doi:10.18388/abp.2015_1089

Koster, K. L., Webb, M. S., Bryant, G., and Lynch, D. V. (1994). Interactions between soluble sugars and POPC (1-palmitoyl-2-oleoylphosphatidylcholine) during dehydration: vitrification of sugars alters the phase behavior of the phospholipid. *Acta – Biomembr.* 1193, 143–150. doi:10.1016/0005-2736(94)90343-3

Langevin, D., and Monroy, F. (2014). Marangoni stresses and surface compression rheology of surfactant solutions. Achievements and problems. *Adv. Colloid. Interf. Sci.* 206, 141–149. doi:10.1016/j.cis.2014.01.006

Le Roux, A. L., Quiroga, X., Walani, N., Arroyo, M., and Roca-Cusachs, P. (2019). The plasma membrane as a mechanochemical transducer. *Phil. Trans. R. Soc. B* 374, 20180221. doi:10.1098/rstb.2018.0221

Lheveder, C., Meunier, J., and Henon, S. (2000). "Brewster angle microscopy," in *Physical Chemistry of biological interfaces*. Editors A. Baszkin and W. Norde (New York City: Marcel Dekker Inc.).

Liehn, H. D., Franco, P. A., Hampel, H., and Hofrichter, G. (1972). A toxicological study of extractum *Hippocastani* semen (EHS). *Panminerva Med.* 14, 84–91. PMID: 4681124.

Lipowsky, R. (1991). The conformation of membranes. *Nature* 349, 475–481. doi:10.1038/349475a0

Liu, Z., and Kim, C. (2020). Deformation analysis of lipid membranes subjected to general forms of intra-membrane viscous flow and interactions with an elliptical-cross-section substrate. *Sci. Rep.* 10, 478. doi:10.1038/s41598-019-57179-z

Loew, D., Schrödter, A., Schwankl, W., and März, R. W. (2000). Measurement of the bioavailability of aescin-containing extracts. *Methods Find. Exp. Clin. Pharmacol.* 22, 537–542. doi:10.1358/mf.2000.22.7.802264

López, D. J., Egido-Gabas, M., López-Montero, I., Busto, J. V., Casas, J., Garnier, M., et al. (2012). Accumulated bending energy elicits neutral sphingomyelinase activity in human red blood cells. *Biophys. J.* 102, 2077–2085. doi:10.1016/j.bpj.2012.03.020

López-Montero, I., Arriaga, L. R., Monroy, F., Rivas, G., Tarazona, P., and Vélez, M. (2008). High fluidity and soft elasticity of the inner membrane of *Escherichia coli* revealed by the surface rheology of model Langmuir monolayers. *Langmuir* 24, 4065–4076. doi:10.1021/la703350s

López-Montero, I., Catapano, E. R., Espinosa, G., Arriaga, L. R., Langevin, D., and Monroy, F. (2013). Shear and compression rheology of Langmuir monolayers of natural ceramides: solid character and plasticity. *Langmuir* 29, 6634–6644. doi:10.1021/la400448x

López-Montero, I., Monroy, F., Vélez, M., and Devaux, P. F. (2010). Ceramide: from lateral segregation to mechanical stress. *Biochim. Biophys. Acta – Biomembr.* 1798, 1348–1356. doi:10.1016/j.bbamem.2009.12.007

Lorent, J. H., Quetin-Leclercq, J., and Mingeot-Leclercq, M. P. (2014). The amphiphilic nature of saponins and their effects on artificial and biological membranes and potential consequences for red blood and cancer cells. *Org. Biomol. Chem.* 12, 8803–8822. doi:10.1039/c4ob01652a

Marsh, D. (1996). Lateral pressure in membranes. *Biochim. Biophys. Acta - Biomembr.* 1286, 183–223. doi:10.1016/S0304-4157(96)00009-3

Mathivet, L., Cribier, S., and Devaux, P. F. (1996). Shape change and physical properties of giant phospholipid vesicles prepared in the presence of an AC electric field. *Biophys. J.* 70, 1112–1121. doi:10.1016/S0006-3495(96)79693-5

Mell, M., Moleiro, L. H., Hertle, Y., López-Montero, I., Cao, F. J., Fouquet, P., et al. (2015). Fluctuation dynamics of bilayer vesicles with intermonolayer sliding: experiment and theory. *Chem. Phys. Lipids* 185, 61–77. doi:10.1016/j.chemphyslip.2014.11.005

Miyakoshi, M., Tamura, Y., Masuda, H., Mizutani, K., Tanaka, O., Ikeda, T., et al. (2000). Antiyeast steroidal saponins from *Yucca schidigera* (Mohave Yucca), a new anti-food-deteriorating agent. *J. Nat. Prod.* 63, 332–338. doi:10.1021/np9904354

Monroy, F., Giermanska-Kahn, J., and Langevin, D. (1998). Dilational viscoelasticity of surfactant monolayers. *Colloids Surfaces A* 143, 251–260. doi:10.1016/S0927-7757(98)00373-2

Muñoz, M. G., Monroy, F., Ortega, F., Rubio, R. G., and Langevin, D. (2000). Monolayers of symmetric triblock copolymers at the air−water interface. 2. Adsorption kinetics. *Langmuir* 16, 1094–1101. doi:10.1021/la9901433

Mussel, M., and Schneider, M. F. (2019). It sounds like an action potential: unification of electrical, chemical and mechanical aspects of acoustic pulses in lipids. *J. R. Soc. Interface* 16, 20180743. doi:10.1098/rsif.2018.0743

Penfold, J., Thomas, R. K., Tucker, I., Petkov, J. T., Stoyanov, S. D., Denkov, N., et al. (2018). Saponin adsorption at the air-water interface-neutron reflectivity and surface tension study. *Langmuir* 34, 9540–9547. doi:10.1021/acs.langmuir.8b02158

Pethica, B. A. (1955). The thermodynamics of monolayer penetration at constant area. Part 1. *Trans. Faraday Soc.* 51, 1402. doi:10.1039/TF9555101402

Philips, R., Ursell, T., Wiggins, P., and Sens, P. (2009). Emerging roles for lipids in shaping membrane-protein function. *Nature* 459, 379–385. doi:10.1038/nature08147

Pittler, M. H., and Ernst, E. (2012). Horse chestnut seed extract for chronic venous insufficiency. *Cochrane Database Syst. Rev.* 11, Cd003230. doi:10.1002/14651858.CD003230.pub4

Rahimi, M., and Arroyo, M. (2012). Shape dynamics, lipid hydrodynamics, and the complex viscoelasticity of bilayer membranes. *Phys. Rev. E* 86, 011932. doi:10.1103/PhysRevE.86.011932

Salassi, S., Caselli, L., Cardellini, J., Lavagna, E., Montis, C., Berti, D., et al. (2021). A Martini coarse grained model of citrate-capped gold nanoparticles interacting with lipid bilayers. *J. Chem. Theory Comput.* 17, 6597–6609. doi:10.1021/acs.jctc.1c00627

Santiago, J. A., Chacón-Acosta, G., and Monroy, F. (2019). Membrane stress and torque induced by frank's nematic textures: A geometric perspective using surface-based constraints. *Phys. Rev. E* 100, 012704. doi:10.1103/PhysRevE.100.012704

Santiago, J. A., and Monroy, F. (2020). Mechanics of nematic membranes: euler–lagrange equations, noether charges, stress, torque and boundary conditions of the surface frank's nematic field. *J. Phys. A. Math. Theor.* 53, 165201. doi:10.1088/1751-8121/ab7cff

Schmid, F. (2013). Fluctuations in lipid bilayers. *Biophys. Rev. Lett.* 8, 1–20. doi:10.1142/S1793048012300113

Seifert, U. (1997). Configurations of fluid membranes and vesicles. *Adv. Phys.* 46, 13–137. doi:10.1080/00018739700101488

Serrien, G., Geeraerts, G., Ghosh, L., and Joos, P. (1992). Dynamic surface properties of adsorbed protein solutions: BSA, casein and buttermilk. *Colloids Surf. A* 68, 219–233. doi:10.1016/0166-6622(92)80208-J

Simons, K., and Ikonen, E. (1997). Functional rafts in cell membranes. *Nature* 387, 569–572. doi:10.1038/42408

Singer, S. J., and Nicolson, G. L. (1972). The fluid mosaic model of the structure of cell membranes. *Science* 175, 720–731. doi:10.1126/science.175.4023.720

Singh, M. K., Shweta, H., Khan, M. F., and Sen, S. (2016). New insight into probe-location dependent polarity and hydration at lipid/water interfaces: comparison between gel- and fluid-phases of lipid bilayers. *Phys. Chem. Chem. Phys.* 18, 24185–24197. doi:10.1039/C6CP01201A

Sirtori, C. R. (2001). Aescin: pharmacology, pharmacokinetics and therapeutic profile. *Pharmacol. Res.* 44, 183–193. doi:10.1006/phrs.2001.0847

Smith, A. R., Visioli, F., Frei, B., and Hagen, T. M. (2006). Age-related changes in endothelial nitric oxide synthase phosphorylation and nitric oxide dependent vasodilation: evidence for a novel mechanism involving sphingomyelinase and ceramide-activated phosphatase 2a. *Aging Cell* 5, 391–400. doi:10.1111/j.1474-9726.2006.00232.x

Sollich, P., Lequeux, F., Hébraud, P., and Cates, M. E. (1997). Rheology of soft glassy materials. *Phys. Rev. Lett.* 78, 2020–2023. doi:10.1103/PhysRevLett.78.2020

Sparg, S. G., Light, M. E., and van Staden, J. (2004). Biological activities and distribution of plant saponins. *J. Ethnopharmacol.* 94, 219–243. doi:10.1016/j.jep.2004.05.016

Sprong, H., Van der Sluijs, P., and Van Meer, G. (2001). How proteins move lipids and lipids move proteins. *Nat. Rev. Mol. Cell. Biol.* 2, 504–513. doi:10.1038/35080071

Sreij, R., Dargel, C., Geisler, P., Hertle, Y., Radulescu, A., Pasini, S., et al. (2018). DMPC vesicle structure and dynamics in the presence of low amounts of the saponin aescin. *Phys. Chem. Chem. Phys.* 20, 9070–9083. doi:10.1039/C7CP08027A

Sreij, R., Dargel, C., Moleiro, L. H., Monroy, F., and Hellweg, T. (2017). Aescin incorporation and nanodomain formation in DMPC model membranes. *Langmuir* 33, 12351–12361. doi:10.1021/acs.langmuir.7b02933

Sreij, R., Dargel, C., Schweins, R., Prévost, S., Dattani, R., and Hellweg, T. (2019). Aescin-cholesterol complexes in DMPC model membranes: A dsc and temperature-dependent scattering study. *Sci. Rep.* 9, 5542. doi:10.1038/s41598-019-41865-z

Srivastava, S., Leiske, D., Basu, J. K., and Fuller, G. G. (2011). Interfacial shear rheology of highly confined glassy polymers. *Soft Matter* 7, 1994–2000. doi:10.1039/C0SM00839G

Tse, J. M., Cheng, G., Tyrrell, J. A., Wilcox-Adelman, S. A., Boucher, Y., Jain, R. K., et al. (2012). Mechanical compression drives cancer cells toward invasive phenotype. *Proc. Nat. Acad. Sci.* 109, 911–916. doi:10.1073/pnas.1118910109

Underland, V., Sæterdal, I., and Strømme Nilsen, E. (2012). Cochrane summary of findings: horse chestnut seed extract for chronic venous insufficiency. *Glob. Adv. Health Med.* 1, 122–123. doi:10.7453/gahmj.2012.1.1.018

Van Meer, G., Voelker, D. R., and Feigenson, G. W. (2008). Membrane lipids: where they are and how they behave. *Nat. Rev. Mol. Cell. Biol.* 9, 112–124. doi:10.1038/nrm2330

Vorselen, D., Van Dommelen, S. M., Sorkin, R., Roos, W. H., Schiller, J., Döpp, S. T., et al. (2018). The fluid membrane determines mechanics of erythrocyte extracellular vesicles and is softened in hereditary spherocytosis. *Nat. Commun.* 9, 4960. doi:10.1038/s41467-018-07445-x

WH de Jeu (1980). *Physical properties of liquid crystalline materials*. 1. Philadelphia, Pennsylvania, United States: Gordon and Breach Science.

Wu, S. H., Sankhagowit, S., Biswas, R., Wu, S., Povinelli, M. L., and Malmstadt, N. (2015). Viscoelastic deformation of lipid bilayer vesicles. *Soft Matter* 11, 7385–7391. doi:10.1039/c5sm01565k

Xu, H., Zhou, S., Tang, Q., Xia, H., and Bi, F. (2020). Cholesterol metabolism: new functions and therapeutic approaches in cancer. *Biochim. Biophys. Acta Rev. Cancer* 1874, 188394. doi:10.1016/j.bbcan.2020.188394